Quaternary Research (2025), 1–25
doi:10.1017/qua.2024.36

Research Article

Preliminary paleoenvironmental analysis and luminescence dating of upper Middle Pleistocene permafrost deposits of the Ulakhan Sular Formation, Adycha River, east Siberia

Julian B. Murton[a], Thomas Opel[b], Phillip Toms[c], Jamie Wood[c], Kseniia Boxleitner[d], Grigoriy Savvinov[e], Petr Danilov[e], Vasily Boeskorov[e], Tomasz Goslar[f,g], Gareth Rogers[h], Aleksei Lupachev[i] and Yana Tikhonravova[j]

[a]Permafrost Laboratory, Department of Geography, University of Sussex, Brighton, BN1 9RH, UK; [b]Alfred Wegener Institute, Helmholtz Centre for Polar and Marine Research, Telegrafenberg A45, 14473 Potsdam, Germany; [c]Luminescence Dating Laboratory, School of Natural and Social Sciences, University of Gloucestershire, Swindon Road, Cheltenham GL50 4AZ, UK; [d]Max Planck Institute of Geoanthropology, 07745 Jena, Germany; [e]Science Research Institute of Applied Ecology of the North, North-East Federal University, 43 Lenin Avenue, Yakutsk 677007, Russia; [f]Adam Mickiewicz University, Faculty of Geographical and Geological Sciences, 61-680 Poznań, Poland; [g]Poznan Radiocarbon Laboratory, Poznań Science and Technology Park, 61-612 Poznań, Poland; [h]Previous address: CGG Robertson, Tyn Y Coed, Llandudno, LL30 1SA, North Wales, UK; Current address: 8 Glanffrydlas, Bethesda, Gwynedd, LL57 3PF, Wales, UK; [i]Institute of Physico–Chemical and Biological Problems in Soil Science, Russian Academy of Sciences, 2/2 Institutskaya, Puschino, 142290, Russia and [j]Melnikov Permafrost Institute, Siberian Branch, Russian Academy of Sciences, 36 Merzlotnaya, Yakutsk, 677010, Russia

Abstract

Ulakhan Sular provides one of the largest natural stratigraphic sections through ancient permafrost deposits in the Batagay–Betenkes region of the Yana Uplands of western Beringia, but their depositional environment, age, and paleoenvironmental significance are uncertain. To address these uncertainties, we report the results of reconnaissance observations of the stratigraphy, sedimentology, paleosols and soil-like bodies, plant and insect macrofossils, and geochronology of the permafrost deposits at the stratotype section of the Ulakhan Sular Formation. Sedimentologically, this formation is dominated by well-sorted, fine to very fine sand that contains fluvial, aeolian, and permafrost sedimentary structures consistent with deposition near the paleo-Adycha River. The fluvio-aeolian deposits have similarities and differences to periglacial fluvio-aeolian and aeolian deposits in modern arctic regions of Canada and Greenland, and Pleistocene deposits in Alaska, China, and northwest Europe. The remarkable thickness of aeolian deposits (~50 m) at Ulakhan Sular is attributed to abundant local sand sources, ample accommodation space, and intensive aeolian transport and deposition. Optically stimulated luminescence dating of quartz sand and post-infrared–infrared dating of K-feldspar sand suggests deposition of the Ulakhan Sular Formation during late Marine Oxygen Isotope Stage (MIS) 6 or MIS 5. The aeolian sand-sheet deposits are correlated with other cold-climate aeolian sand and silt (loess) deposits in Beringia and southern Siberia, indicating a regional episode of aeolian sand transport and deposition at a similar time to glaciation by the Eastern Siberian Ice Sheet.

Keywords: Fluvio-aeolian sand deposits, western Beringia, ice wedges, luminescence dating, syngenetic permafrost, radiocarbon dating, Siberia, sand wedges

Introduction

The ancient permafrost of Beringia provides a remarkable archive of Pleistocene paleoenvironmental conditions, often preserving exceptionally well the frozen remains of terrestrial ecosystems. The permafrost archive, however, has often proved difficult to date beyond the range of radiocarbon methods (e.g., Wetterich et al., 2019; Murton et al., 2022). Additionally, recognition of aeolian deposits (loess, sand sheets, and dunes) has often been contentious (e.g., Lea and Waythomas, 1990), with deposition attributed to water (e.g., Rampton, 1988, p. 42; Schirrmeister et al., 2020, 2025), despite strong geologic arguments that windblown deposits accumulated extensively in Beringia (Tomirdiaro, 1980, 1982; Hopkins, 1982; Péwé and Journaux, 1983; Astakhov, 2014; Murton et al., 2015). Significantly, aeolian deposits offer the potential to interpret ice-age atmospheric conditions (e.g., wind directions or relative wind speeds) and therefore to test reconstructions from Earth-system models and identify and evaluate Pleistocene landforms in arctic and subarctic regions, for example relict dune fields in western arctic North America (Carter, 1981; Dallimore et al., 1997) and central Yakutia (Galanin, 2021), as well as yardangs. Periglacial aeolian deposits are also suitable for applying luminescence dating methods (Bateman, 2008). As a result, aeolian sedimentary sequences frozen in permafrost represent a valuable target for paleoenvironmental analysis, as we show from the site of Ulakhan Sular, in arctic Russia.

Corresponding author: Julian B. Murton; Email: j.b.murton@sussex.ac.uk

Cite this article: Murton JB *et al* (2025). Preliminary paleoenvironmental analysis and luminescence dating of upper Middle Pleistocene permafrost deposits of the Ulakhan Sular Formation, Adycha River, east Siberia. *Quaternary Research* 1–25. https://doi.org/10.1017/qua.2024.36

Ulakhan Sular provides one of the largest natural exposures of permafrost in the Batagay–Betenkes region of the uplands of the Yana drainage basin, eastern Siberia (Kaplina et al., 1983). At Ulakhan Sular, sandy permafrost deposits up to ~55 m thick crop out almost continuously for more than 2 km along the outer bend of a meander of the Adycha River right bank. The site has long been known as an important source of Pleistocene vertebrate bones (e.g., Sher et al., 2011; Germonpré et al., 2017). However, the age of the Ulakhan Sular Formation is uncertain, with suggestions ranging from Middle Pleistocene to Late Pleistocene (Kaplina et al., 1983; Sher et al., 2011; Vdovina and Skuba, 2013a, 2013b). Thus, the paleoenvironmental significance of this formation to reconstructing environmental conditions in Beringia is unclear.

Here we report the results of reconnaissance observations of the stratigraphy, sedimentology, ground ice, paleosols and soil-like bodies, plant and insect macrofossils, and geochronology of ancient permafrost deposits at the stratotype section of the Ulakhan Sular Formation, at Ulakhan Sular (67.69°N, 135.73°E; Fig. 1). Our aims are to determine its age and evaluate its regional paleoenvironmental significance, particularly in western Beringia. Our objectives are to (1) describe and interpret the stratigraphy and sedimentology of the Ulakhan Sular Formation, (2) report

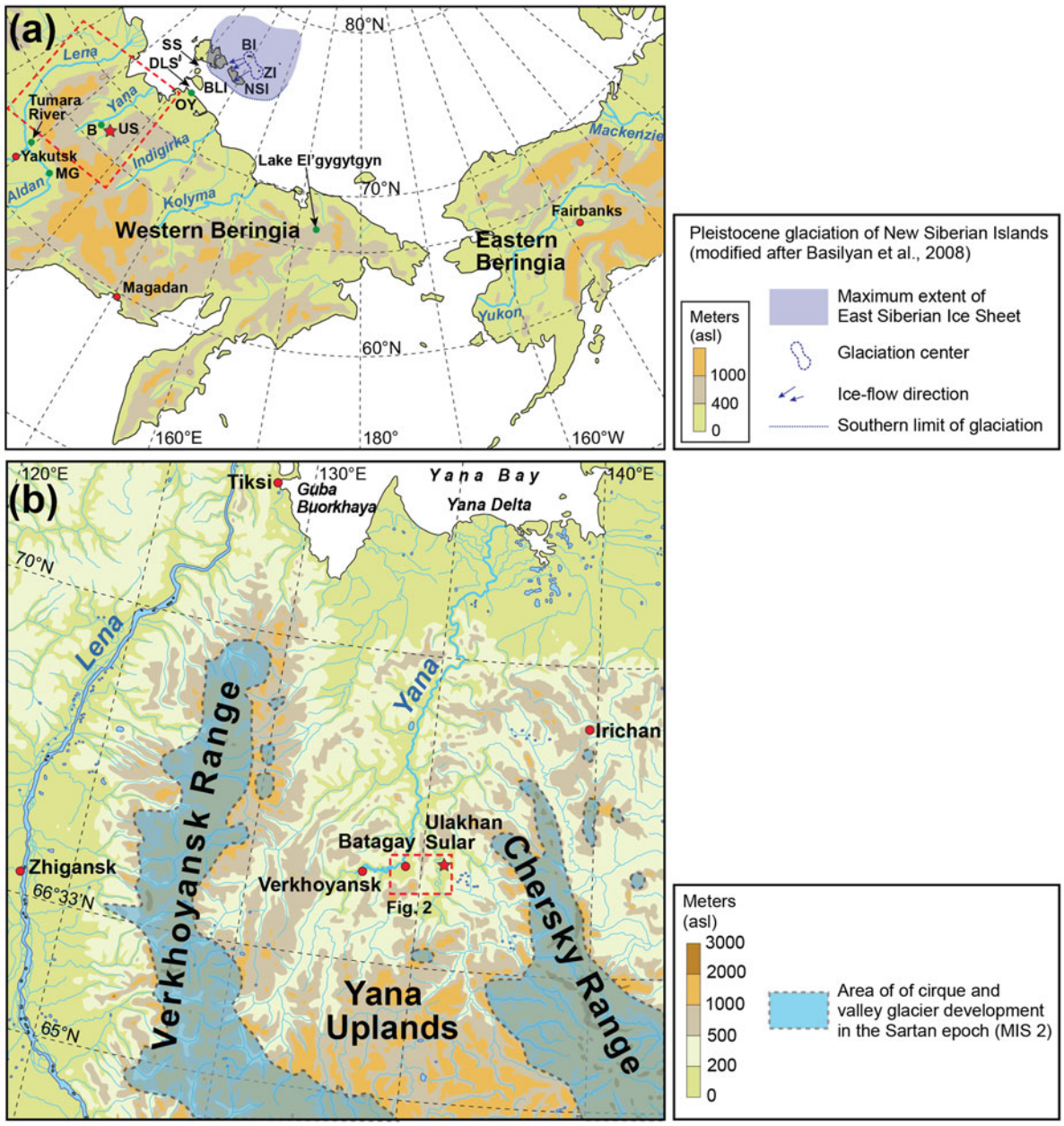

Figure 1. (a) Location map of Beringia. B, Batagay megaslump; BI, Bennett Island; BLI, Bol'shoy Lyakovsky Island; DLS, Dmitry Laptev Strait; MG, Mamontova Gora; OY, Oyogos Yar; SS, Sannikov Strait; US, Ulakhan Sular; ZI, Zhokhov Island. Mauve shading shows reconstructed maximum extent of glacial ice of the East Siberian Ice Sheet (modified from Basilyan et al., 2008). Red dashed box shows location of panel (b). (b) Location map showing the topographic setting of Ulakhan Sular within the Adycha River basin, northern Yakutia. Glacial limits during the last (Sartan) glaciation, according to Glushkova (2011), are indicated. Red dashed box shows location of Figure 2. Modified from Murton et al. (2022).

https://doi.org/10.1017/qua.2024.36 Published online by Cambridge University Press

the first luminescence ages from this formation, and (3) correlate the deposits with others from Beringia.

Study Area

The Pliocene and Quaternary deposits of the Batagay–Betenkes study area are dominated by sand, silt, and gravel attributed to alluvial, lacustrine, and colluvial deposition (Fig. 2) in an environment with forest or tundra–steppe vegetation. The lithostratigraphy, paleoenvironmental interpretation, and suggested age of Pliocene and Pleistocene deposits in the study area are listed in Table 1 and detailed in Supplementary text 1. Below we summarize the descriptions and interpretations of the Ulakhan Sular Formation.

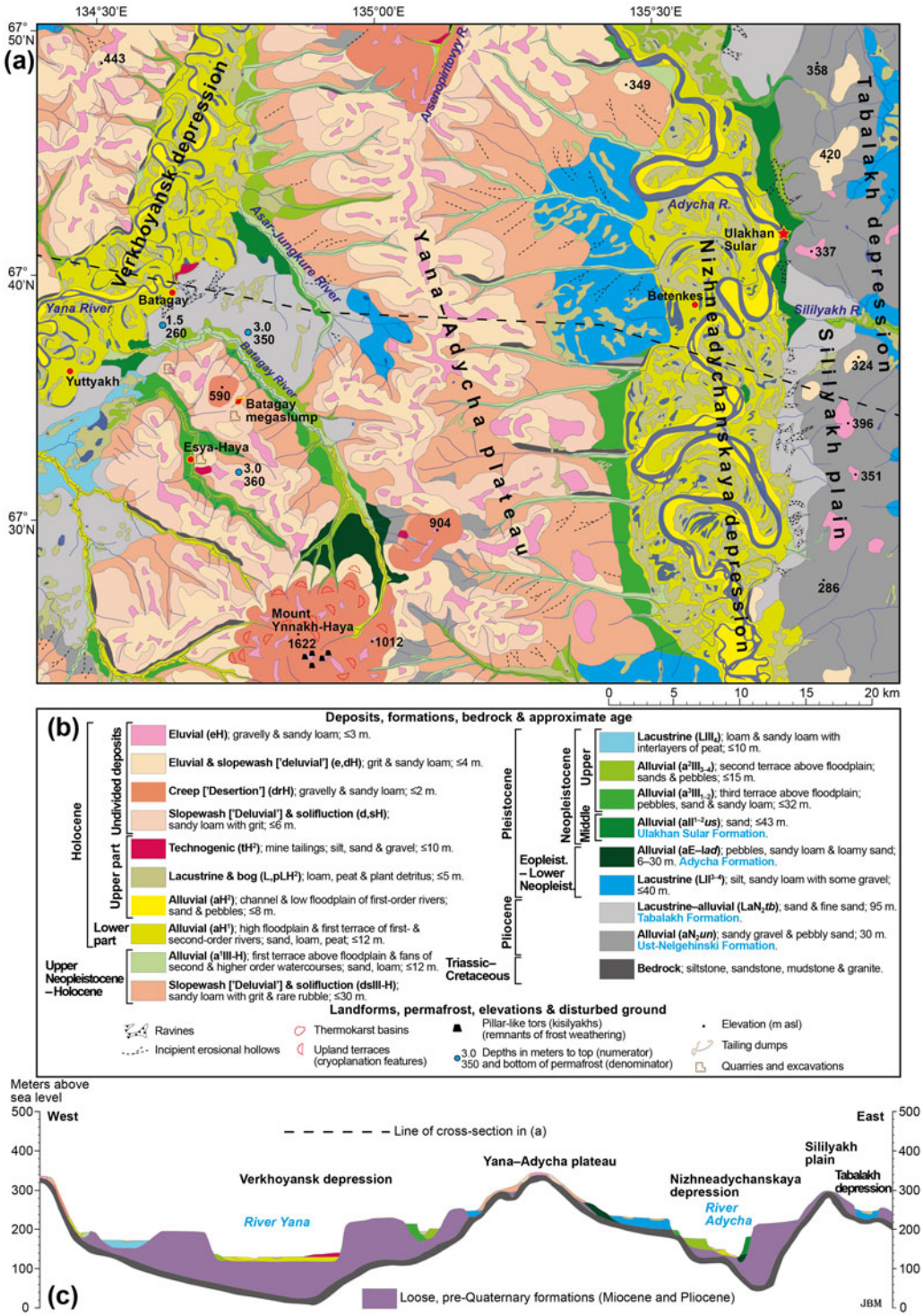

Figure 2. (a) Geological map of Quaternary and Pliocene deposits, generalized bedrock, and landforms in the Batagay–Betenkes region of the uplands of the Yana drainage basin. (b) Legend. (c) Schematic geologic cross section running west to east from near Batagay to near Ulakhan Sular. The section extends some distance east and west of the map shown in (a). Redrawn and modified from Vdovina (2002a, 2002b) and Vdovina and Skuba (2013a).

https://doi.org/10.1017/qua.2024.36 Published online by Cambridge University Press

Table 1. Lithostratigraphy, sedimentology, organic material, interpretation, and age of the Miocene to Pleistocene sedimentary sequence in the Batagay–Betenkes study area.[a]

Lithostratigraphic units or deposits, abbreviation, thickness	Sedimentology	Organic material	Paleoenvironmental interpretation	Age suggestions (A, B, etc.)
12. **Deluvial–solifluctional deposits (dsIII-H)** (usually 5–10 m; ≤30 m)	Sandy loam and some angular rock debris			Last glacial–interglacial transition
11. **Alluvial deposits (a^1III-H)** (≤12 m)	Sand and loam, pebbly near the base	Peaty near top; pollen and spores of green mosses, *Betula nana* and *Alnus* spp. dominate		Last glacial–interglacial transition
10. **Lacustrine deposits ($laIII_4$)** (≤10 m)	Loams and sandy loams	Intercalated peat		~MIS 2 (29–11.7 ka)
9. **Alluvial deposits of the second terrace above the floodplain ($a^2III_{3–4}$)** (≤15 m)	Sandy to pebbly	Spores, pollen	Tundra–steppe vegetation associated with a cold climate	~MIS 4 (72–58 ka)–MIS 3 (58–29 ka)
8. **Alluvial deposits of the third terrace above the floodplain ($a^3III_{1–2}$)** (≤32 m)	Gravel overlain by sand and sandy loam	Spores, pollen, vertebrate remains	*Larix gmelinii* forest and sparse *Picea* areas before climate cooling and drying led to tundra–steppe vegetation	~MIS 5 (132–72 ka)–MIS 3 (58–29 ka)
7. **Ulakhan Sular Formation ($aII^{1–2}$*us*)** (≤43 m)	Mainly sands with lenses of gravel	Spores and pollen of green mosses and grasses, with some *Artemisia* sp. and *B. nana*; soil-like bodies with grass and sedge root remnants; *Mammuthus primigenius*, *Bison priscus*, *Rangifer tarandus*, *Equus caballus*	Alluvial deposits. Tundra–steppe vegetation and areas of shrub–steppe vegetation associated with a cold, dry climate	(A) ~MIS 11 (429–365 ka) and MIS 10 (365–337 ka) (B) Middle Pleistocene to early Late Pleistocene (Kaplina et al., 1983; Sher et al., 2011) (C) Kazantsev interglacial (MIS 5) and Zyrian (MIS4: 72–58 ka) (reviewed in Kaplina et al., 1983)
6. **Adycha Formation (aE–l*ad*)** (6–30 m thick)	Sandy loam to loamy sand with abundant pebbles	Spores, pollen; *E. caballus*, *B. priscus*, *Castor fiber; Lepus* spp., *Lemmus obensis*, *Microtus* spp.; bivalve shells	Alluvial deposits. Light coniferous forest with a mix of *Pinus* and *Betula* spp.	(A) Eopleistocene to lower Neopleistocene (≤2.58 or 1.8 Ma; ≥~429 ka / MIS 12) (B) ESR ages of 360 ± 17 ka (MIS 11–10) and 212 ± 10 ka (MIS 7–6) on bivalve shells (Nikolskiy, 2010; Lee et al., 2015) (C) Normal polarity sediments attributed to Brunhes Chron (0.78–0 Ma) (Minyuk and Ivanov, 2011)
5. **Lacustrine deposits ($lII_{3–4}$)** (≤40 m)	Silt and sandy loam with some gravel	Plant remains and peat lenses; spores and pollen of green mosses, sedges, *Artemisia*, and mixed grass	Exceptionally cold and relatively dry conditions existed when one or more extensive lakes formed	(A) ~MIS 9 (337–279 ka) and MIS 8 (279–243 ka) Vdovina and Skuba (2013a, 2013b) (B) Older than Adycha Formation because lacustrine deposits were incised prior to deposition of Adycha Formation (see Fig. 2c and Supplementary text 1). (This study)
4. **Tabalakh Formation (LaN_2*tb*)** (≤95 m)	Mostly sand and fine sand	Spores, pollen	Lacustrine and alluvial deposits. Potentially a major sand source for younger deposits.	Pliocene

3. **Ust-Nelgehinski Formation (aN_2un)** (≤30m)	Mainly sandy gravel and pebbly sand	Spores, pollen	Alluvial deposits. Coniferous forest of *L. gmelinii* and *Pinus* or mixed forest, with unforested areas	Pliocene
2. **Malyshov Formation** (≤34 m)	Pebbly gravel, pebbly sand and pebbly loam	Spores, pollen	Alluvial deposits. Dark coniferous forests with patches of deciduous and broad-leaved trees associated with moderately warm and humid conditions	Miocene
1. **Magyar Formation** (usually 3–10 m; ≤30 m)	Rock fragments with interstitial clay; rounded pebbles in ancient thalwegs	Spores, pollen	Alluvial–slope deposits. Dark *Picea* and *Juniperus* forests with patches of *Betula* spp. and broad-leaved species	Miocene

[a]Stratigraphy based on Vdovina and Skuba (2013a, 2013b). Ages are also based on these authors unless otherwise indicated.
Abbreviations: ESR, electron spin resonance; MIS, marine oxygen isotope stage.

The Ulakhan Sular Formation is mostly sand, and contains gravel lenses and soil-like bodies (Kaplina et al., 1983; Vdovina and Skuba, 2013a, 2013b). Large vertebrate bones from it include *Mammuthus primigenius*, *Bison priscus*, *Rangifer tarandus*, and *Equus caballus* (Grigoriev et al., 2017). Spores and pollen from it suggest that no significant restructuring of the vegetation pattern occurred during sedimentation; instead, open herbaceous landscapes (steppe, meadow, and tundra) persisted, indicating a dry continental climate. The formation occurs mainly near Ulakhan Sular, and also in the valley of the Asar-Jungkure River, and to the southwest of Batagay (Fig. 2a). The formation is thought to be alluvial in origin, deposited by the ancestral rivers Adycha, Asar-Jungkure, Tuostakh, and Yana. Its age is contentious, with suggested ages ranging from mid Middle Pleistocene—broadly equivalent to Marine Oxygen Isotope Stage (MIS) 11 (~429–365 ka)—to early Late Pleistocene, possibly Zyrian (MIS 4: ~72–58 ka) near the top (Table 1, Supplementary text 1).

The climate of the study area is strongly continental, with very cold (–45 to –50°C average monthly winter temperatures) and long winters with little snow, and short, relatively warm summers (+12 to +15°C average monthly temperatures) (Vdovina and Skuba, 2013b). Mean annual precipitation at Batagay is ~200 mm (Murton et al., 2023). Air masses that form above Siberia throughout the year strongly impact the seasonal variability of climate. Winter (September to March) is influenced by a high-pressure air cell—the Siberian anticyclone, with its main center above Mongolia—that stretches beyond the Verkhoyansk Mountains and forms another pressure peak above the Yana Uplands, contributing to the development of southerly and southwesterly winds with low average monthly wind velocities (0.5–1.0 m/s). In summer (May–August), the southwest Asian low-pressure system dominates the region. It contributes to development of northern and northwestern winds with higher-than-winter average monthly wind velocities (2.5 m/s with maximum of 5 m/s) (USSR Climate Digest, 1989). Permafrost is continuous, with thicknesses of ~260–360 m beneath the Yana–Adycha plateau near Batagay (Fig. 2a). Active-layer depth varies between ~0.2 and 2.5 m, according to ground conditions.

The sections examined in this study are located along the eastern margin of the Nizhneadychanska depression and the western margin of the Sililyakh plain (Fig. 2a). The depression contains the Holocene meander belt (up to ~12 km wide) of the Adycha River. The sections truncate the eroding, right, outer bend of a meander measuring ~2 km east–west and north–south. Fluvial scroll bars deposited by lateral accretion on the opposite (inner) side of the bend, to the west, indicate that the meander has migrated to the east, northeast, and north during recent times (Fig. 3b).

Methods

Stratigraphy, sedimentology, and soils

The stratigraphy and sedimentology of four stratigraphic sections were examined along the eastern bluff of the Adycha River at Ulakhan Sular during August 2017. The sections formed a north–south transect ~2 km long (Fig. 3, Supplementary Tables 1–4). Some additional observations of modern soils, paleosols, soil-like bodies, and ice wedges near the upper part of the outcrop were made during July 2023. IUSS Working Group WRB (2022) was used for soil description.

https://doi.org/10.1017/qua.2024.36 Published online by Cambridge University Press

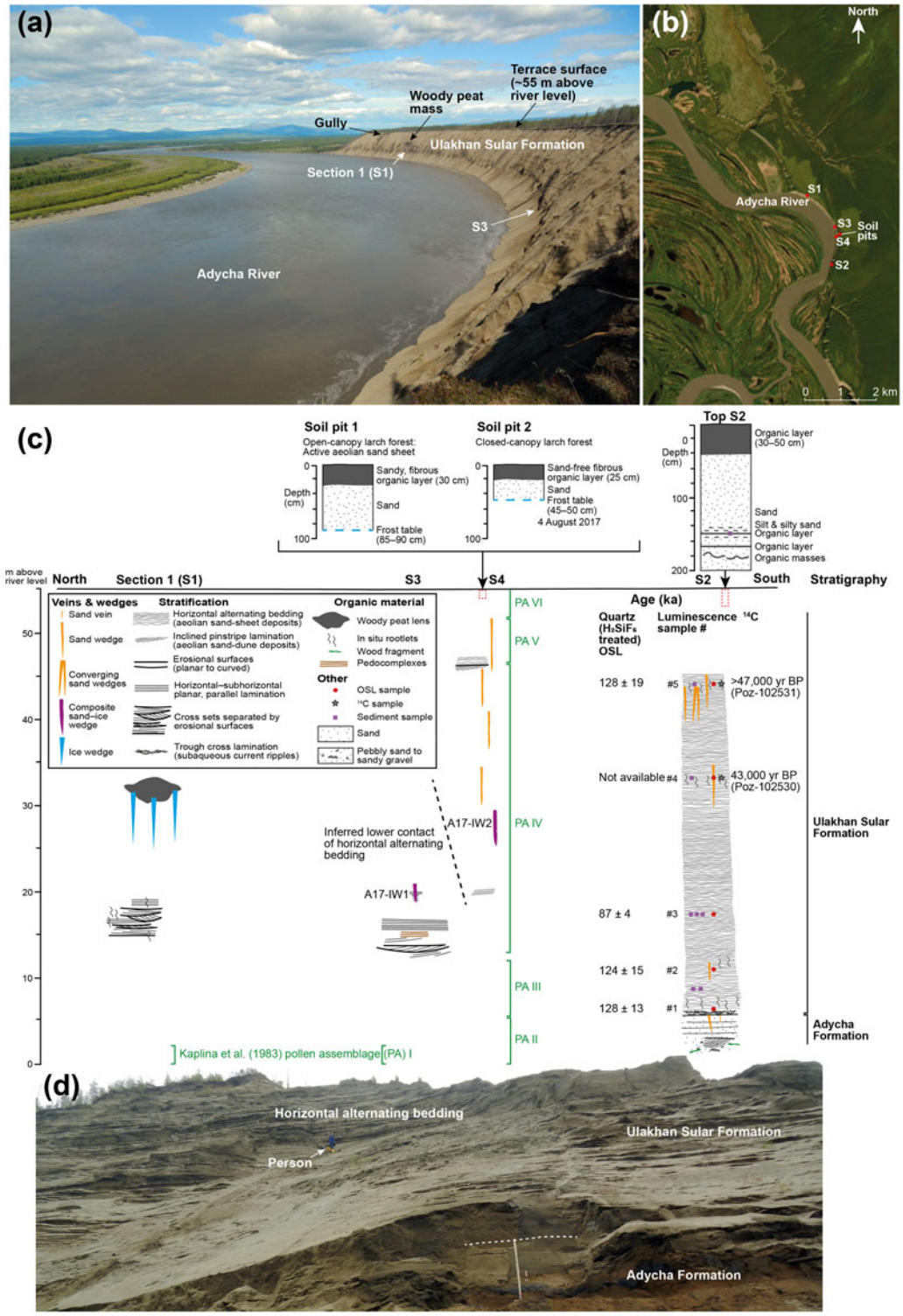

Figure 3. Section locations and stratigraphy at Ulakhan Sular. (a) Photograph of Ulakhan Sular bluff and terrace beside Adycha River, viewed towards the north from near section 4, with approximate locations of sections 1 and 3 (S1 and S3) marked. (b) Satellite image from Arctic DEM showing locations of sections 1–4 (S1–S4) and soil pits. (c) Schematic stratigraphy and sedimentology for S1–4 and soil pits located in (b). Approximate depths of Kaplina et al.'s (1983) pollen assemblages are indicated in green. (d) Photograph of Adycha Formation beneath Ulakhan Sular Formation. Dashed white line indicates their contact. Person for scale. Photographs (a) and (d) by Julian Murton.

Vertical heights above river level and/or depth below the bluff top were determined by tape measure and corrected by trigonometry. Sections were cleaned of slumped sediment with a spade and trowel, and the freshly exposed material was compared with adjacent dried sediment that often revealed details of sedimentary structures wind-etched in sand. In addition, two soil pits were dug inland of the top of section 4 to determine the near-surface stratigraphy and the depth of the frost table. Pit 1 was beneath open-

https://doi.org/10.1017/qua.2024.36 Published online by Cambridge University Press

canopy larch forest ~60 m inland of the bluff edge, and pit 2 beneath closed-canopy larch forest ~150 m inland of the bluff edge.

A second site was briefly visited to provide a Holocene reference example of alluvium from the actively eroding bank of a small cutoff channel of the Adycha River (67.66°N, 135.69°E; 138 m above sea level), ~3 km upstream of the Ulakhan Sular exposures. The sediments comprise organic-rich silty sands (Fig. 4).

Sediment physical and chemical properties

The physical and chemical properties of sediment from the Ulakhan Sular Formation were determined to characterize the stratigraphic unit and to identify if any vertical trends were present. Section 2 was selected for sampling because it was possible to ascend it from river level to bluff top and therefore to sample stratigraphically throughout the formation. Eight samples of sediment were collected (Fig. 3c). Two samples—one from 6.3 m above river level (arl), the other from 10.8 m arl—were mislabeled and are therefore both given a nominal height of 8.55 m arl, midway between them. Particle size was determined by a laser diffraction particle analyzer (Malvern Mastersizer 3000). Sand percentages were calculated for particle-size ranges between 66.9 and 2000 µm, and silt percentages between 5.21 and 58.9 µm. Magnetic susceptibility (MS), a proxy for the sediment content of magnetizable minerals, was measured by a Bartington Instruments MS2 equipped with an MS2B sensor. High-frequency MS data are expressed in units of 10^{-8} m^3/kg. The total elemental carbon (TC) and nitrogen (TN) contents were measured with a VARIO-EL-III Element Analyzer, and total organic carbon content (TOC) was measured with a VARIO MAX C Analyzer. Gravimetric ice content was determined on one frozen sample of sand obtained by drilling.

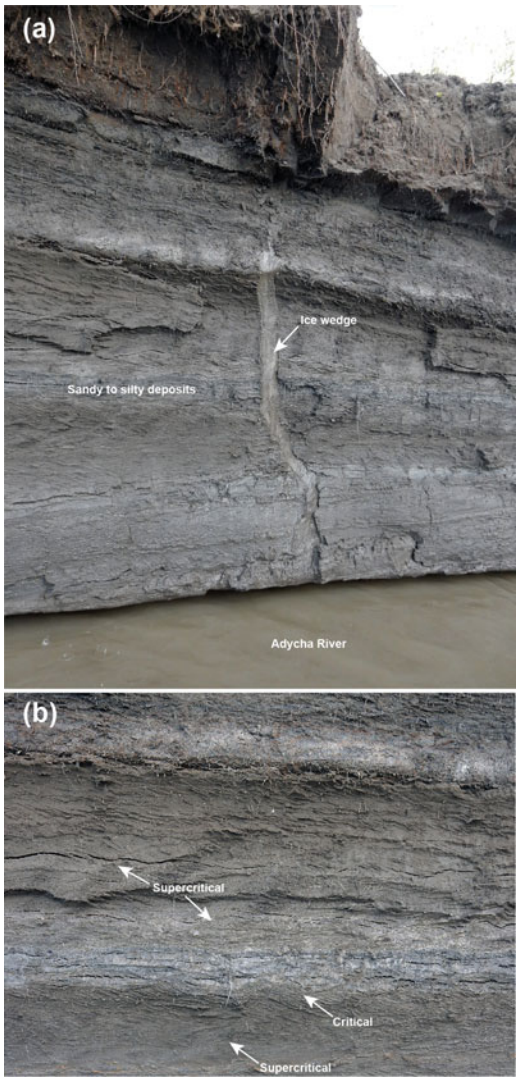

Figure 4. Holocene alluvium exposed in a vertical section beside the Adycha River, ~3 km upstream of the Ulakhan Sular exposures. (a) Narrow ice wedge in stratified sandy to silty deposits. River at base. Vertical distance ~5 m high. (b) Climbing-ripple cross lamination (mostly supercritical angles of climb, some critical) formed by subaqueous climbing ripples. Vertical distance ~0.7 m high. Photographs (a) and (b) by Kseniia Boxleitner.

Ground-ice stable isotope geochemistry

We sampled two composite wedges at the bluff of Ulakhan Sular (A17-IW1 from section 3, and A17-IW2 from section 4; Fig. 3c) and one ice wedge (A17-IW3) in a riverbank at the Holocene alluvium site (Fig. 4a). Additionally, we took samples of supernatant water from two sediment samples. All melted samples were stored cool in completely filled, 30 mL narrow-mouth plastic bottles. The oxygen ($\delta^{18}O$) and hydrogen (δD) stable isotope composition was measured with a Finnigan MAT Delta-S mass spectrometer (1σ is better than 0.1‰ for $\delta^{18}O$ and 0.8‰ for δD; Meyer et al., 2000). Values are given as per mil (‰) difference from the Vienna Standard Mean Ocean Water (VSMOW) standard. The deuterium excess (d) is calculated as $d = \delta D - 8\delta^{18}O$ (Dansgaard, 1964).

Mineralogy

The mineralogy (including light and heavy minerals) of eight samples of sediment, seven from the Ulakhan Sular Formation (Sed_1 to Sed_7) and one from directly above it (Sed_8), was determined using a Quanta 650F Scanning Electron Microscope, utilizing the QEMSCAN® automated mode of operation. QEMSCAN® provides digital imaging and quantitative mineralogical and petrological data. The method enables vast amounts of chemical and mineralogical data to be processed from a range of widely available samples. It also provides particle-size and particle-angularity measurements. Sample preparation and analysis are detailed in Supplementary text 2.

Luminescence dating

Five samples of sand for luminescence dating were collected from the Ulakhan Sular Formation at section 2, along a vertical transect upwards from 48.3 m depth (near the base of the formation) to 11.2 m depth (near the top) (Fig. 3c). A metal cylinder was pushed into freshly thawed and undisturbed sediments, all from the same facies (horizontal alternating bedding, as described below). The samples were shielded immediately from sunlight, sealed tightly, and then stored cool until analysis. One sample of sand was obtained in frozen condition by drilling a hole adjacent to luminescence sample GL17113 (A17-S2-OSL3) in order to measure the gravimetric water (ice) content of the sand in undisturbed permafrost. The water content obtained from this sample

https://doi.org/10.1017/qua.2024.36 Published online by Cambridge University Press

(22.6%) was adopted for calculation of all luminescence ages. The sample preparation and measurements are detailed in Supplementary text 2.

Plant macrofossil and insect analyses

Samples for plant macrofossil and insect analysis were taken from the cleaned bluff sections using a trowel; each sample was labeled, placed individually into a cotton bag for air-drying, and remained otherwise unprocessed. In the archaeobotanical laboratory of the Max Planck Institute for the Science of Human History in Jena, Germany, the samples were wet-sieved with standard geologic test sieves from Rentsch GmbH with mesh sizes of 2.00 and 0.25 mm and then air-dried. We screened the samples using a Leica S9i stereo microscope and hand-picked material suitable for macrofossil and insect identification. Photomicrographs of the selected taxa were taken with a Keyence digital microscope VHX 6000.

^{14}C dating

Organic remains were collected from two samples of sand from the Ulakhan Sular Formation. Sample A17-S2-AMS6 (Lab. number Poz-102530) comprised fine in situ roots from a depth of 22.1 m below the ground surface (bgs), and sample A17-S2-AMS7 (Lab. number Poz-102531) comprised fine in situ roots and rhizomes from a depth of 11.2 m bgs. The roots and rhizomes were assumed to have grown soon after deposition of the host sand, which is attributed below to incremental aggradation of aeolian sand sheets. The samples were selected for dating because they were the two highest stratigraphic samples in the sequence, and therefore assumed to be the youngest and the most likely to be within the range of radiocarbon dating. The sand samples were dried for two days at ~30°C in an oven and then the roots and rhizomes were picked by tweezer from the sand. Each sample comprised multiple fragments of roots and/or rhizomes. The two samples were prepared and analyzed in the "Compact Carbon AMS" spectrometer at the Adam Mickiewicz University in Poznan (for details see Murton et al., 2015). A third sample of plant remains (rootlets and Gmelin larch, *Larix gmelinii*, needle) from the riverbank at the Holocene reference site was dated at the AWI MICADAS ^{14}C dating facility (for details see Mollenhauer et al., 2021).

The ^{14}C results are presented as $F^{14}C$ values (Reimer et al., 2004), and conventional radiocarbon ages are given in years before present (yr BP). Ages within the calibration range were calibrated to years before present (cal yr BP), i.e., before 1950 CE, using Calib 8.20 (Stuiver and Reimer, 1993) and the IntCAL20 data set (Reimer et al., 2020). Calibrated ages are rounded to the nearest 10 years.

Results

Stratigraphy and sedimentology

The Ulakhan Sular Formation was examined in four stratigraphic sections along a horizontal distance of ~2 km (Fig. 3b). Sections 1 and 3 (in the northern, upstream part of the bluff) differ sedimentologically from sections 2 and 4 (in the southern, downstream part). Their details are presented in Figures 5–7 and Supplementary Tables 1–4, and summarized below.

Section 1 contains well-stratified, fine–medium sand. Stratification types are (1) horizontal–subhorizontal, planar parallel lamination (Supplementary Fig. 3); (2) trough cross sets ~0.5–1.5 m thick, some with well-developed, concave-up basal erosion surfaces (Fig. 5a); and (3) tabular cross sets up to at least 1.5 m thick (Supplementary Fig. 3). Truncation surfaces, including a reactivation surface, are numerous. The pore-ice-cemented sediments contain relatively few in situ roots, mostly isolated or in clumps. A prominent lens of black, wood-rich organic material forms an isolated body ~15 m wide and up to 5 m thick above a lower contact with a relief of 2–3 m, i.e., infilling a depression downcut into the sand (Fig. 5g). Wood fragments are up to at least 10 cm in diameter and a few meters in length. Ice wedges up to a few tens of centimeters in apparent width and up to a few meters high occur within and adjacent to the wood-rich lens (Fig. 6e). Section 3 contains massive to stratified sand with planar parallel to cross lamination. Some brown, horizontal organic layers to lenses a few millimeters to 3 cm thick are present (Fig. 5f), and in situ roots, some delicate, are abundant in the sand. A composite sand–ice wedge up to 15 cm wide and more than 1.5 m high is also present (Fig. 6d).

Sections 2 and 4 are dominated by horizontal alternating bedding (HAB), with subsidiary pinstripe lamination. The HAB comprises gray fine sand and dark gray silty sand that is well stratified (Figs. 5c–d and 6a–c). Strata are horizontal–subhorizontal, planar to gently undulating to wavy, and 0.5 cm to several centimeters thick. In situ roots and rhizomes, some woody, are abundant throughout the HAB. Multiple sand wedges occur at different stratigraphic levels (Fig. 6a–c), and related structures include composite sand–ice wedges and a sand vein. The sand wedges are a few centimeters to 30 cm wide, and up to at least several meters high, some with a distinctive chimney-like appearance (Fig. 6c). Pinstripe lamination in gently dipping foresets occurs in section 4 (e.g., at 20 and 46 m arl; Fig. 3c). The upper 2 m of section 2 comprise sand, silty sand, and silt, and contain horizontal parallel strata a few millimeters to 2 cm thick (Figs. 3c and 5h). Prominent is a black cryoturbated organic layer. Mollusc remains up to a few millimeters long (cf. *Pisidium* spp.) are abundant in dark gray silt to silty sand, dark brown organic layers, and gray sand. Modern aeolian sand-sheet deposits occur in two soil pits excavated ~60–150 m inland of the bluff top near section 4 (Supplementary Figs. 2b and c).

The visually distinctive HAB appears to taper out towards the ground surface between sections 4 and 3 (Fig. 3c). This indicates that the HAB in sections 2 and 4 stratigraphically overlies and is therefore younger than the less clearly stratified deposits of sections 1 and 3.

Ice wedges

Two stratigraphic levels of ice wedges were observed in 2023 in the upper 10 m of the Ulakhan Sular Formation near sections 3 and 4 (Figs. 3b and 6f). The lower level contains yellowish–brown ice wedges up to 2–3 m wide within woody and organic-rich deposits with a concave-upward form and hosting segregated ice lenses 15–25 cm thick. The wedges penetrate underlying sand with a buried soil interbed that contains ferruginous spots and streaks. The upper level comprises milky white ice wedges up to 5 m high within sand containing ice lenses. Some white ice wedges penetrate underlying yellowish–brown ice wedges.

Ice wedges separated by blocks of mineral ground ~5–6 m in diameter were also observed in 2023, ~50–70 m south of section

https://doi.org/10.1017/qua.2024.36 Published online by Cambridge University Press

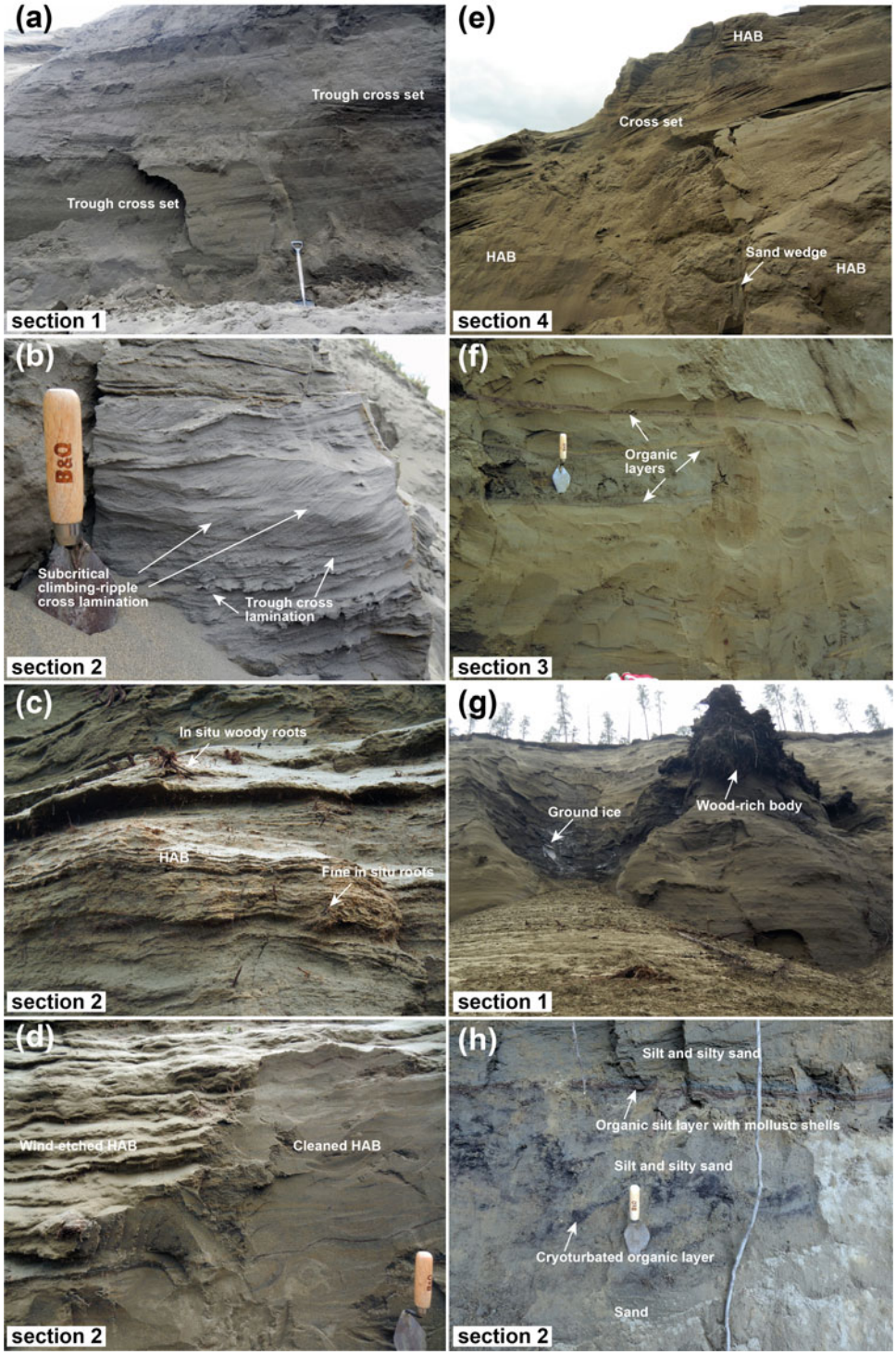

Figure 5. Sedimentary facies within the Ulakhan Sular Formation (a–g) and above it (h). (a) Trough cross sets (subaqueous dune deposits), section 1. Spade for scale. (b) Subcritical climbing-ripple cross lamination (subaqueous climbing-ripple deposits) beneath OSL 1 sample location, section 2. Trowel for scale. (c) Horizontal alternating bedding (HAB; aeolian sand-sheet deposits) and in situ roots and rhizomes, some woody, section 2. Vertical distance is ~1 m high. (d) HAB, wind-etched on left, showing in situ roots versus cleaned section on right, section 2. Trowel for scale. (e) Cross set (aeolian dune deposit). HAB underlies and overlies the cross set, and contains a sand wedge, section 4. Pinstripe lamination (not shown) occurs in a second cross set to right of image. Vertical distance is ~7 m high. (f) Pedocomplex, marked by three organic layers 1–3 cm thick, section 3. Trowel for scale. (g) Irregular body of wood-rich organic material surrounded by sand, section 1. Vertical distance is ~40 m high. (h) Silty deposit containing organic and cryoturbated layers above Ulakhan Sular Formation, section 2. Vertical distance is ~1 m high. Photographs (a), (c), (d)–(g) by Julian Murton; (b) by Thomas Opel; (h) by Kseniia Boxleitner.

2, beside a thermoerosional gully ~15–20 m wide and ~20 m deep (Fig. 7). The ice wedges are milky to light-yellowish, 2–3 m or more high and their tops ~2 m and 20–30 cm wide; the former represent primary wedges, the latter secondary wedges. The top of one primary ice wedge borders a former thermoerosional channel and cave infilled with peaty sediments

https://doi.org/10.1017/qua.2024.36 Published online by Cambridge University Press

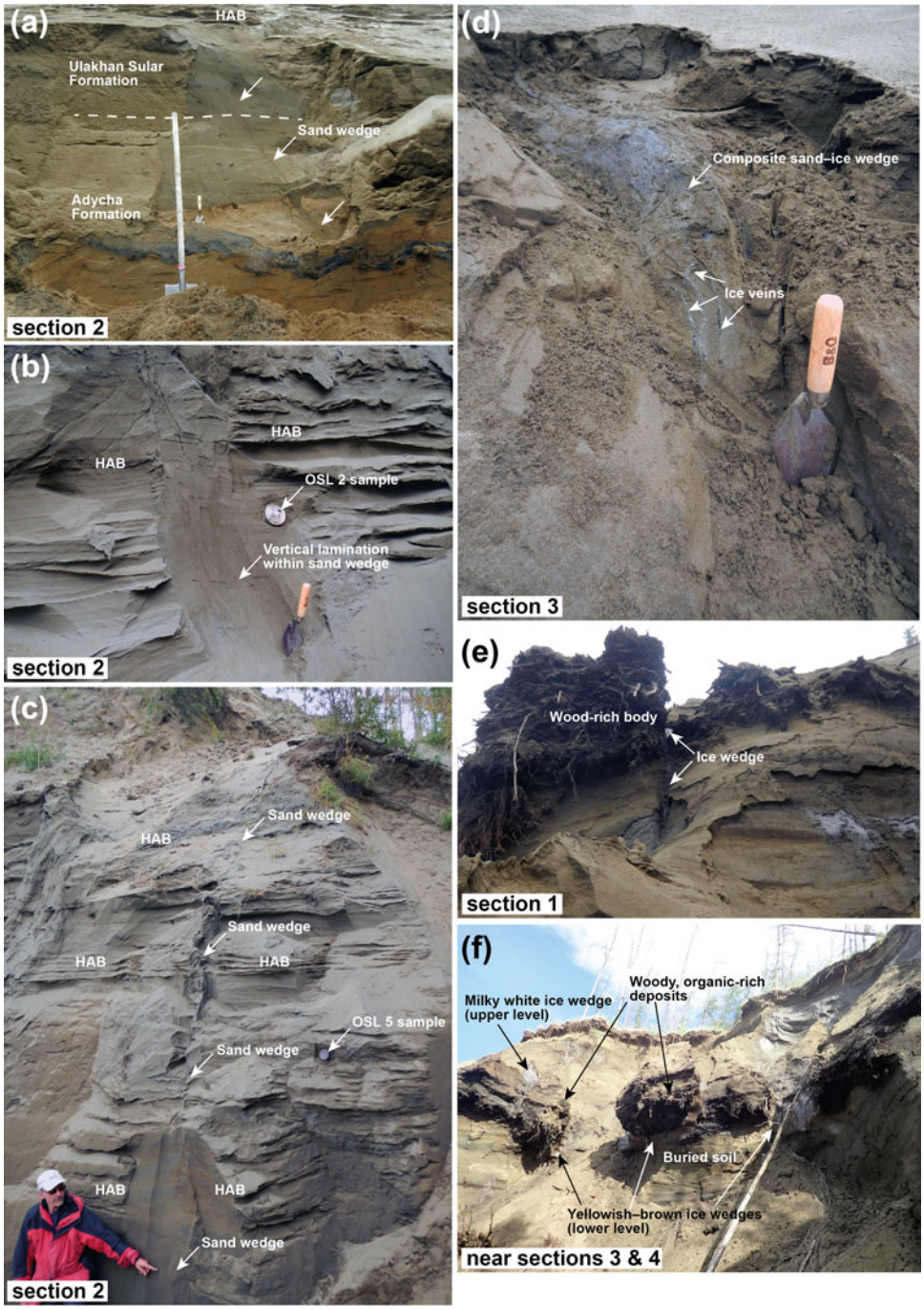

Figure 6. Cryogenic veins and wedges within the Ulakhan Sular Formation. (a) Sand wedge (marked by arrows) extending down from the basal part of the formation into the underlying Adycha Formation, section 2. Dashed line marks sharp contact between them. Spade for scale. (b) Sand wedge within horizontal alternating bedding (HAB) beside optically stimulated luminescence (OSL) 2 sample location, section 2. Trowel for scale. (c) Narrow, chimney-like sand wedge ~4 m high in HAB beside OSL 5 sample location, section 2. (d) Composite sand–ice wedge, with three ice veins indicated, section 3. Trowel for scale. (e) Ice wedge beside wood-rich body, section 1. Vertical distance ~5 m high. (f) Upper part of the Ulakhan Sular Formation (around sections 3 and 4) with two stratigraphic levels of ice wedges. Vertical distance 20–25 m high. Photographs (a), (d) and (e) by Julian Murton; (b) and (c) by Thomas Opel; and (f) by Yana Tikhonravova.

in the top part. The outer edges of the wedge are colored by ferruginous materials and the top probably melted during the formation of the thermoerosional gully. The ground between the wedges contains at least seven subhorizontal organic-rich layers full of well-preserved peaty material, shrub remnants, wood stems, trunks, and parts of stumps. The layers vary in thickness from 5–15 cm to 50–60 cm and are interlayered with slightly gleyic dark gray sandy material (40–50 cm thick) containing relatively small (few millimeters diameter) grass and sedge root remnants. A single ice lens 5 cm thick is observed between peaty layers four and five. Both organic-rich and sandy layers curve upwards adjacent to the ice wedges, which indicates the simultaneous processes of ice wedge formation and deposition of these layers in presumably boggy, overmoistured conditions, possibly along with local episodes of solifluction or creep.

https://doi.org/10.1017/qua.2024.36 Published online by Cambridge University Press

Figure 7. Near-surface organic layers and ice wedge, all likely of Holocene age. Visible part of ice wedge ~2 m high. Photograph by Yana Tikhonravova.

Sediment properties

The particle size of the Ulakhan Sular Formation is dominated by very fine to fine sand (median values of 104–131 µm), with the proportions of sand (67–2000 µm) and silt (5–59 µm) being 80.9–90.3% and 6.0–15.7%, respectively (Fig. 8). By contrast, the uppermost sample, directly above the Ulakhan Sular Formation, is silt-rich (red line in Fig. 8b), with a median value of 35 µm, comprising 65.5% silt and 23.0% sand. Similarly, QEMSCAN analyses gave a modal grain size of 125–250 µm (fine sand), except the uppermost sample (Sed_8), with a modal size of 16–31 µm (medium silt). Sixty-seven percent of quartz grains are well-rounded in sample Sed_8, compared to only 17–27% for all other samples (Fig. 9d). High-frequency MS values range from 13.9 to 19.6×10^{-8} m^3/kg, increasing to 23.3×10^{-8} m^3/kg in the uppermost sample. TC contents are 0.4–0.8%, peaking at 1.7% at the top, TN contents are <0.1% (0.2% at top), and TOC contents are <0.1% (1.1% at top). A single value of 22.6% for gravimetric water content was obtained from frozen sand 17.1 m arl.

Stable isotopes

Although the composite wedges show very similar $\delta^{18}O$ values of around –32‰, their δD values differ significantly (around –235 and –258‰, respectively), leading to contrasting *d* values (around –2 and 18‰) (Fig. 10, Supplementary Table 5). Pore ice stable isotope values of samples Sed_1 and Sed_8 scatter between –28 and –22‰ in $\delta^{18}O$, –209 and –170‰ in δD, and 5 and 15‰ in *d* and are hard to interpret. Samples of ice wedge A17-IW3 (mean $\delta^{18}O$: –29.0‰, mean δD: –226.3‰, mean *d*: 5.5‰) from the Holocene reference riverbank plot along the Global Meteoric Water Line (GMWL).

Mineralogy

The bulk mineralogy of the eight sand samples is dominated by quartz (~40–50% volume) (Fig. 9, Supplementary Table 6). The quartz content of Sed_8 (directly above the Ulakhan Sular Formation) comprises 65% sub-65 µm grains, whereas for all other samples (i.e., from the Ulakhan Sular Formation) this is only 16–25%. Plagioclase feldspar comprises ~18–19%, and K-feldspar is ~6–7% volume, except for sample Sed_8 (1.5 m bgs), with ~4% volume. Muscovite is more common than biotite across all samples, and illite is the dominant clay mineral. Sample Sed_8 contains a significantly higher volume of illite and kaolinite in comparison to the other samples. Calcite and dolomite are consistently low across all samples (<2% volume, respectively). The heavy mineralogy of the samples is also relatively consistent in the samples, except for Sed_8 (Fig. 9, Supplementary Table 7). This sample contains a slightly higher volume of heavy minerals, due to a higher volume of rutile, apatite, and olivine.

Plant macrofossils and insects

Four samples were studied for the plant macrofossil and insect analysis: one from the Ulakhan Sular Formation, one from the un-named silty deposit above it, and one each from the Adycha Formation and Holocene alluvium (Supplementary Table 8, Figs. 11 and 12). Plant remains are most abundant in sample A17-K-05 (1.7 m bgs, on top of the Ulakhan Sular Formation at section 2), indicating woodland vegetation with ponds and lakes in forest clearings. Identification of insect remains reported taxa characteristic of terrestrial and aquatic environments. Sample A17-K-07, a composite from the main body of the Ulakhan Sular Formation at section 2, provided only non-identifiable rootlets. Sample A17-K-03, from the Holocene riverbank alluvium of the Adycha River (~2 m bgs), contained plant remains of woodland taxa. Sample A17-K-06, from the Adycha Formation ~3 m arl or ~3 m below its upper contact with the Ulakhan Sular Formation, comprised only remains of plants that are of broad ecological tolerance, and therefore cannot be used for

https://doi.org/10.1017/qua.2024.36 Published online by Cambridge University Press

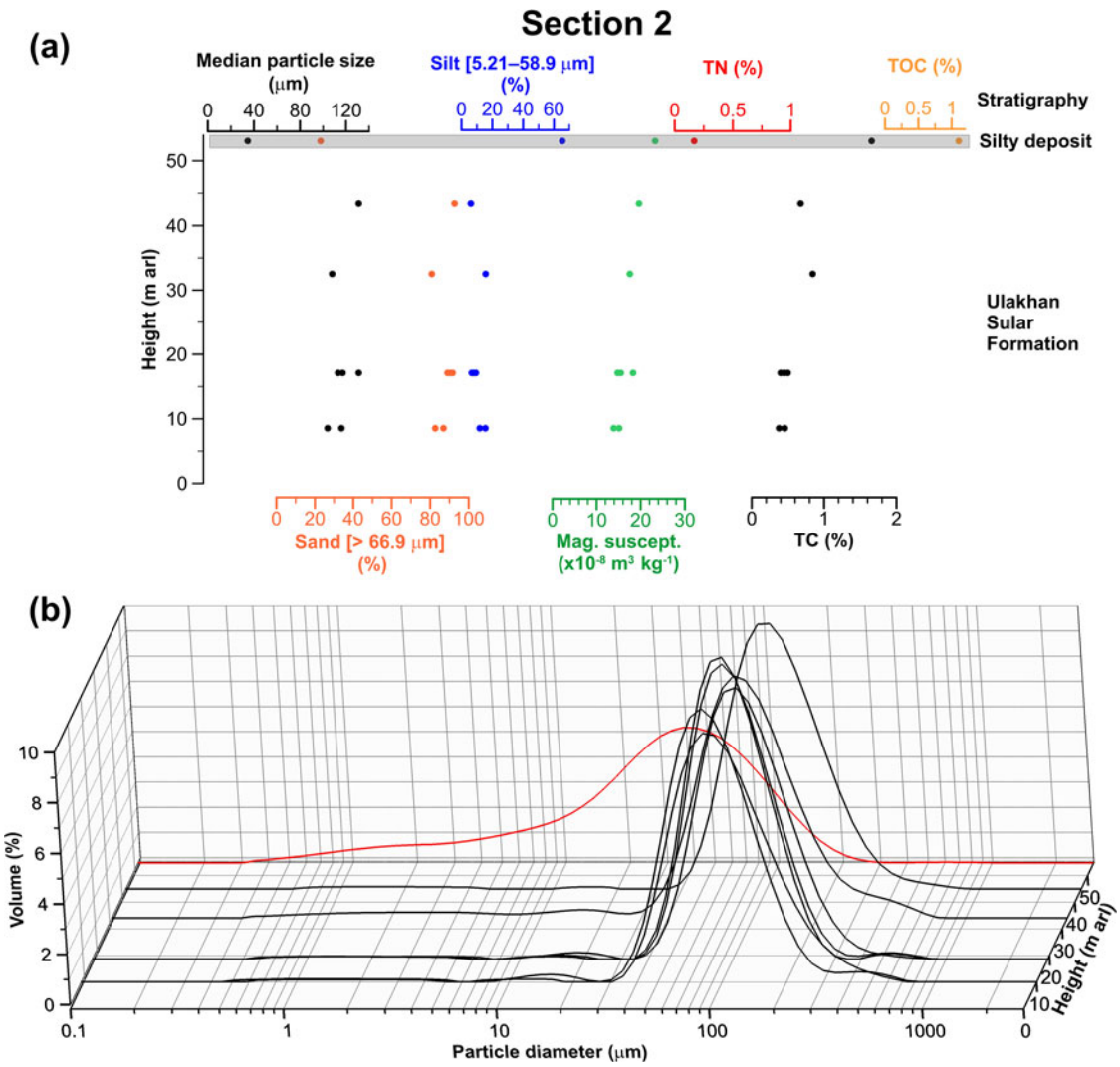

Figure 8. (a) Sedimentary properties and (b) particle-size distributions plotted against height through section 2, Ulakhan Sular. TN (total elemental nitrogen) and TOC (total organic carbon) values of <0.1% are not plotted for the lower seven samples. TC, total elemental carbon. The silty deposit on top of the Ulakhan Sular Formation is indicated by the gray rectangle in (a) and the red line in (b). arl, above river level.

environmental reconstruction. However, we identified remnants of insects distinctive to the taiga forest and steppe patches within it (Supplementary text 3).

Luminescence dating

A summary of paired quartz and K-feldspar D_e, D_r, and age data for the five Ulakhan Sular samples from section 2 is presented in Tables 2 and 3, and example data for GL17111 in Figure 13. Quartz aliquots produced a strong response to infrared (IR) stimulation (Fig. 13a) during initial D_e analysis, and most samples produced post-IR optically stimulated luminescence (OSL) ratios of ~0.30 (Table 3). Treatment of the quartz fraction with H_2SiF_6 significantly reduced the infrared-stimulated luminescence (IRSL) signal (Fig. 13b), and post-IR OSL ratios for the subsequent single aliquot regenerative-dose (SAR) measurements were consistent, or close to unity. Unfortunately, there was insufficient material to repeat SAR measurements on GL17114 following H_2SiF_6 treatment. The reduction in contamination by IR-bearing minerals resulted in significant increases in D_e (22–92%) and estimated age. D_e distributions for the H_2SiF_6 treated fractions also displayed a higher degree of overdispersion (31–45%); this is likely driven by the OSL signal being derived from fewer grains per aliquot, given the relative differences in quartz and feldspar sensitivity (Rhodes, 2015), and the onset of saturation (D_0) being significantly lower for the H_2SiF_6 treated quartz isolates (Table 3). All D_e values exceed $2D_0$, the recommended upper limit for accurate D_e determination of quartz (Wintle and Murray, 2006).

Dose recovery experiments demonstrated the ability of quartz aliquots to successfully recover laboratory doses using the SAR protocol, with samples producing dose recovery ratios consistent with unity. Dose recovery ratios for the post-infrared infrared-stimulated luminescence (pIRIR) signals of K-feldspars varied significantly (Table 3, Fig. 13f). For most samples the $pIRIR_{200}$ signal recovered doses that were within 16% of unity; GL17115 was the exception and overestimated the given dose by ~40%. The $pIRIR_{250}$ signal overestimated the given dose in most instances, up to 65%. For both OSL and pIRIR measurements, low and high repeat dose measurements for most samples are statistically consistent with unity, suggesting sensitivity correction was successful for both minerals.

https://doi.org/10.1017/qua.2024.36 Published online by Cambridge University Press

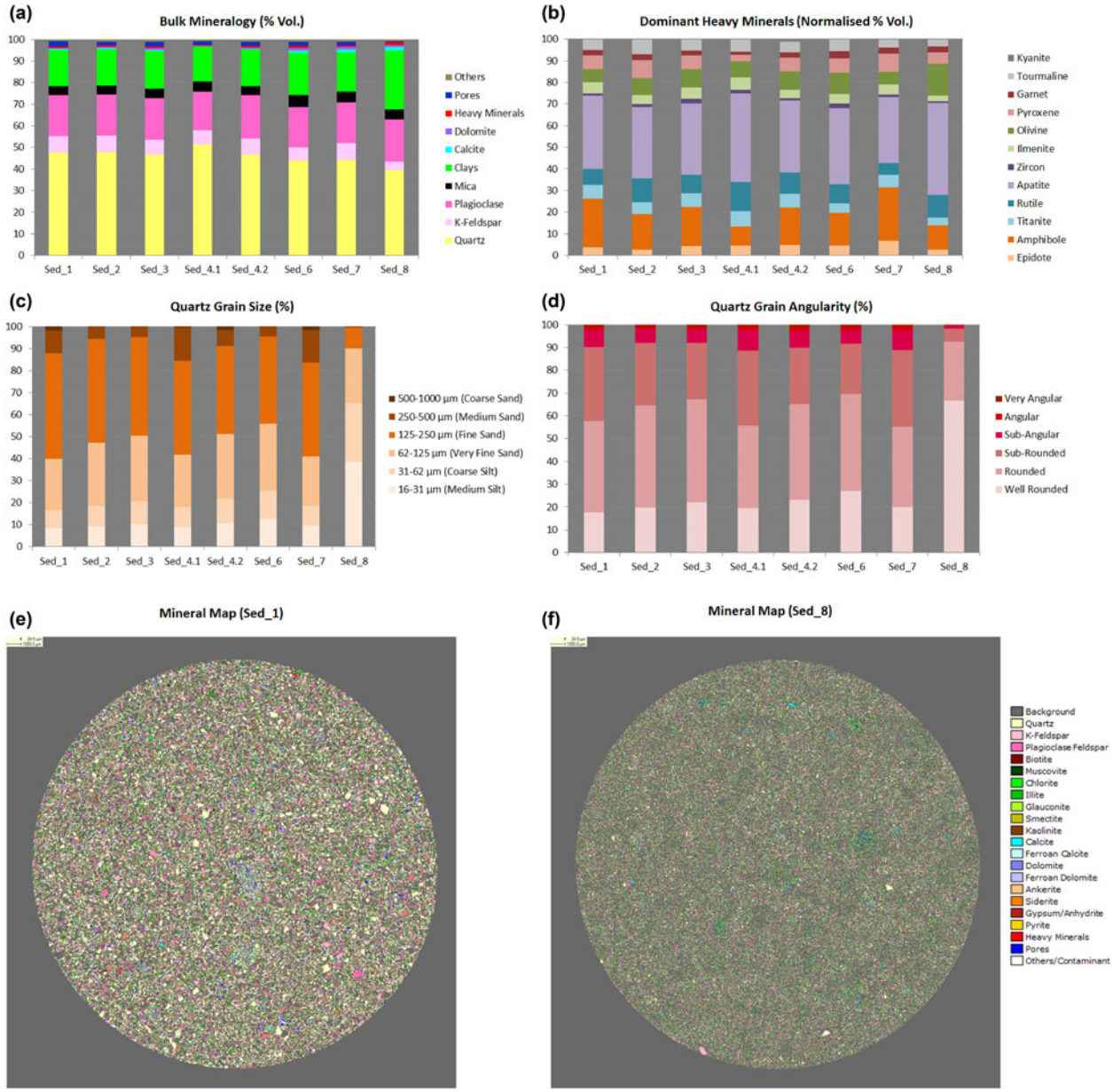

Figure 9. Mineralogical and textural properties of seven sandy samples (Sed_1 to Sed_7) from the Ulakhan Sular Formation and one silty sample (Sed_8) from above it obtained by the QEMSCAN analysis. (a) Bulk mineralogy, (b) dominant heavy minerals, (c) quartz grain size, and (d) quartz grain angularity. Mineral maps of (e) sample Sed_1 and (f) sample Sed_8.

K-feldspar fading tests on GL17111 display a systematic change in *g*-values, with fading rates decreasing with increased IR stimulation temperature (Fig. 13e). Over laboratory timescales the IR_{50} signal experienced significant fading and produced a *g*-value of 6.52 ± 0.93%/decade. The *g*-values for $pIRIR_{200}$ (−0.51 ± 1.14) and $pIRIR_{250}$ (−1.85 ± 1.24%/decade) indicate that the pIRIR signals from GL17111 either experience negligible fading or fading that cannot be accounted for over laboratory timescales. Following 4 h in the solar simulator, ∼12 Gy ($pIRIR_{200}$) and 20 Gy ($pIRIR_{250}$) residual doses were recovered from naturally and laboratory-irradiated aliquots. Given the relatively high D_r values within the Ulakhan Sular sequence, residual dose subtraction would only result in a 5 to 8 ka shift in pIRIR age; this is relatively insignificant considering the age of the deposits and the associated error margins.

Four post-H_2SiF_6 quartz OSL ages were produced for the Ulakhan Sular sequence; three are statistically indistinguishable (GL17111, 128 ± 13 ka; GL17112, 124 ± 15 ka; GL17115, 128 ± 19 ka), whilst sample GL17113 is distinctly younger (87 ± 4 ka). Five K-feldspar $pIRIR_{200}$ and $pIRIR_{250}$ age estimates were also produced for the sequence. $pIRIR_{200}$ and $pIRIR_{250}$ ages for GL17111 (170 ± 12 and 181 ± 24 ka) were statistically indistinguishable, as were those for GL17112 (117 ± 8 and 123 ± 10 ka). There were discrepancies between pIRIR ages for GL17113 (137 ± 8 and 170 ± 12 ka), GL17114 (110 ± 8 and 208 ± 27 ka) and GL17115 (110 ± 7 and 129 ± 8 ka), with $pIRIR_{250}$ estimates producing the greatest ages for each sample. Samples GL17112 and GL17115 produced both $pIRIR_{200}$ and $pIRIR_{250}$ age estimates that were statistically consistent with quartz OSL ages.

https://doi.org/10.1017/qua.2024.36 Published online by Cambridge University Press

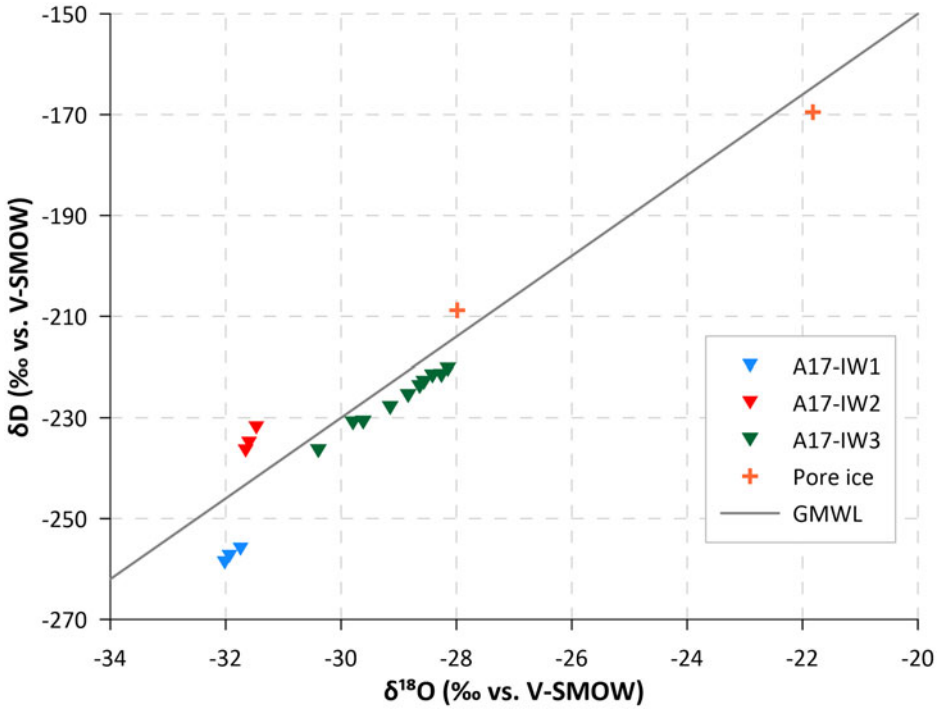

Figure 10. Co-isotope plots of composite wedges (A17-IW1 and A17-IW2) and pore ice from the Ulakhan Sular Formation and an ice wedge (A17-IW3) from Holocene deposits beside the Adycha River.

^{14}C dating

Three ^{14}C ages were obtained (Table 4). An age of 43,000 ± 2000 ^{14}C yr BP was obtained from in situ roots at a depth of 22.1 m bgs in section 2. This provided a calibrated median age of 45,760 cal yr BP, which is near the limit of radiocarbon dating and is probably a minimum age for sand deposition. Second, an age of >47,000 ^{14}C yr BP was obtained from in situ roots and rhizomes at a depth of 11.2 m bgs in section 2. Third, the sample of rootlets and a *L. gmelinii* needle from 2 m bgs at the Holocene reference riverbank was dated to 213 ± 109 ^{14}C yr BP (calibrated median age: 220 cal yr BP).

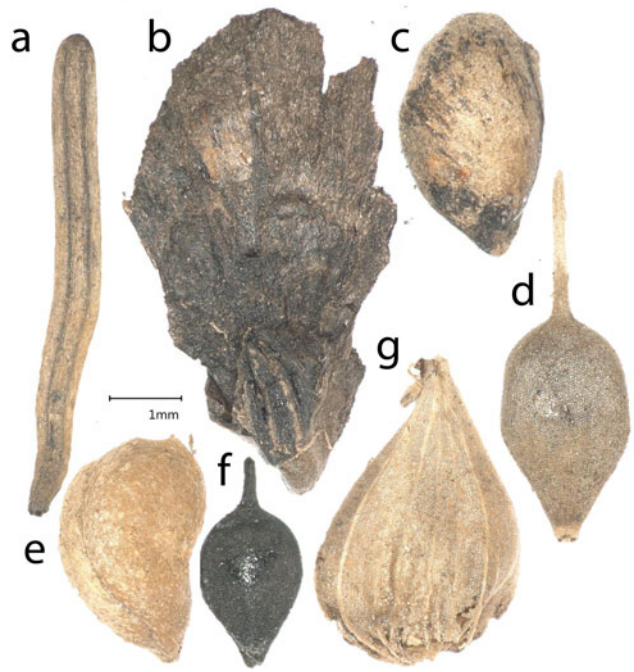

Figure 11. A selection of plant macrofossils recovered from the Ulakhan Sular Formation samples: (a) *Larix gmelinii*, needle; (b) *Larix gmelinii*, cone scale; (c) *Larix gmelinii*, seed; (d) *Carex* cf. *reuteriana*; (e) *Potamogeton* cf. *filiformis*, fruit; (f) *Carex* sect Digitatae; (g) *Carex* sp.. Photomicrographs by Kseniia Boxleitner.

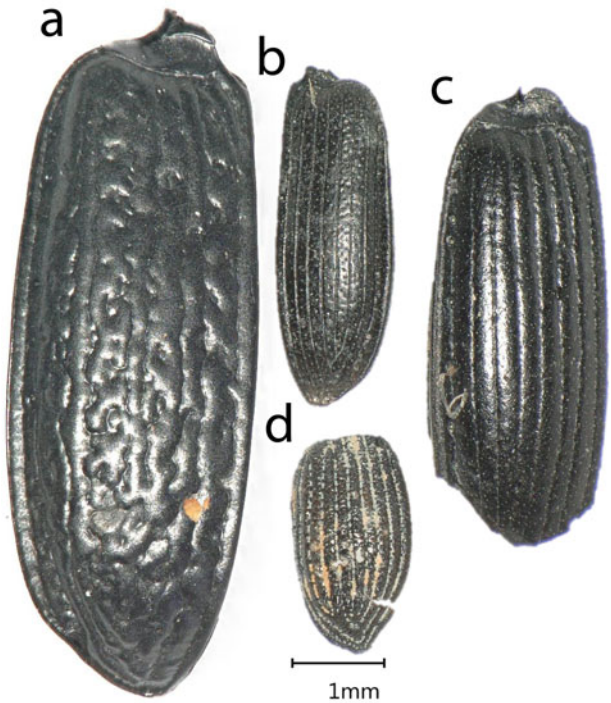

Figure 12. Elytra of (a) *Pterostichus* (*Lenapterus*) *vermiculosus* Men.; (b) *Dicheirotrichus mannerheimii* Sahlb; (c) *Pterostichus* (*Cryobius*) *ventricosus* Esch.; (d) *Ceutorhynchus* sp. Photomicrographs by Kseniia Boxleitner.

https://doi.org/10.1017/qua.2024.36 Published online by Cambridge University Press

Table 2. Dose-rate parameters from 125–180 µm quartz and K-feldspar isolates for luminescence dating from section 2 of the Ulakhan Sular Formation. Cosmic dose rate for ~68°N, 136°E, 135 m above sea level

Lab code	Mineral	Overburden (m)	Gravimetric moisture content (%)	Ge γ-spectrometry (*ex situ*) K (%)	Th (ppm)	U (ppm)	$^{226}Ra/^{238}U$	Internal β D_r (Gy/ka)	External α D_r (Gy/ka)	External β D_r (Gy/ka)	External γ D_r (Gy/ka)	Cosmic D_r (Gy/ka)
GL17115	Quartz	11.2	22.6 ± 2.5	2.10 ± 0.12	7.20 ± 0.50	1.68 ± 0.13	0.89 ± 0.14	-	-	1.51 ± 0.08	0.83 ± 0.04	0.05 ± 0.01
	K-feldspar							0.53 ± 0.10	0.18 ± 0.05			
GL17114	Quartz	22.1	22.6 ± 2.5	1.86 ± 0.11	7.30 ± 0.50	1.83 ± 0.14	1.10 ± 0.17	-	-	1.39 ± 0.08	0.80 ± 0.04	0.02 ± 0.00
	K-feldspar							0.53 ± 0.10	0.19 ± 0.05			
GL17113	Quartz	37.5	22.6 ± 2.5	1.76 ± 0.11	6.71 ± 0.48	1.75 ± 0.13	0.87 ± 0.12	-	-	1.31 ± 0.07	0.75 ± 0.04	0.01 ± 0.00
	K-feldspar							0.53 ± 0.10	0.17 ± 0.05			
GL17112	Quartz	43.8	22.6 ± 2.5	2.11 ± 0.12	7.06 ± 0.49	1.61 ± 0.13	0.94 ± 0.13	-	-	1.51 ± 0.08	0.82 ± 0.04	0.01 ± 0.00
	K-feldspar							0.53 ± 0.10	0.17 ± 0.05			
GL17111	Quartz	48.3	22.6 ± 2.5	1.56 ± 0.10	6.39 ± 0.46	1.58 ± 0.13	0.76 ± 0.13	-	-	1.18 ± 0.07	0.69 ± 0.03	0.01 ± 0.00
	K-feldspar							0.53 ± 0.10	0.16 ± 0.04			

Discussion

Ulakhan Sular Formation

Fluvio-aeolian deposits

We expected the deposits of the Ulakhan Sular Formation to be alluvial based on previous studies by Kaplina et al. (1983; their member 5) and Vdovina and Skuba (2013b), but we unexpectedly identified an additional, major aeolian component. The downstream parts of the Ulakhan Sular Formation (Kaplina et al.'s sections I and II, and our sections 1 and 3) have characteristics of braided-river deposition, whereas the upstream parts (Kaplina et al.'s section III and our sections 2 and 4) are dominantly aeolian.

Channel-belt deposition in a sandy braided river is indicated by sedimentary structures in our sections 1 and 3. Large trough cross sets (Fig. 5a) are attributed to deposition by migrating, sinuous-crested, subaqueous dunes. Large, tabular cross sets (Supplementary Fig. 3) likely formed by deposition at the margins of migrating bars. The reactivation surface within one tabular cross set indicates erosion of foresets preceded renewed foreset deposition, likely driven by changes in river stage change during bar migration. Horizontal–subhorizontal, planar, parallel laminated sand (Supplementary Fig. 3) is interpreted as upper flow regime plane beds deposited during flood conditions. Collectively, these sedimentary structures (Collinson et al., 2006) are characteristic of the channel belt of sandy braided rivers such as the South Saskatchewan River, Canada (Cant and Walker, 1978; Sambrook Smith et al., 2006; Ashworth et al., 2011), the lower Tana River, Norway (Collinson, 1970), the lower Niobrara River, northeast Nebraska (Skelly et al., 2003), and the Platte River, Nebraska (Blodgett and Stanley, 1980).

Aeolian deposition dominant in our sections 2 and 4 is indicated by (1) chimney-like syngenetic sand wedges and composite wedges; (2) HAB; (3) pinstripe lamination; and (4) in situ roots and rhizomes pervasive within HAB—indicating that plants grew more or less at the same time as sand aggraded on the surface, in similar fashion to plant growth during deposition of yedoma silt (Murton et al., 2015). HAB is generally attributed to aeolian deposition on sand sheets whose surface alternated between wet and dry conditions, leading to adhesion of a suspension load of loamy very fine sand, and deposition of a traction load of fine sand, respectively (Lea, 1990). HAB equates with subfacies 2a (sand with horizontal, undulatory stratification) in southwestern Alaska (Lea, 1990) and with aeolian facies from Banks Island (Pissart et al., 1977) and the Tuktoyaktuk Coastlands (Bateman and Murton, 2006) of northwest Canada. It also corresponds with subfacies B of Ruegg (1983), facies 3 of Schwan (1986, 1988), sand-sheet facies B of Koster (1988), alternating bedding of fine sand and loamy very fine sand of Kasse (1997, 2002), wet aeolian sand-sheet deposits/facies B of Schokker and Koster (2004), and wavy horizontal bedding of Kasse and Aalbersberg (2019) from coversand in northwest Europe. The misinterpretation of aeolian sand-sheet deposits as channel or floodplain alluvium in Siberia and Alaska has been noted by Lea and Waythomas (1990). Pinstripe lamination is characterized by thin, inversely graded laminae and attributed to deposition by wind ripples (facies 2a of Lea, 1990). Analytical data on median grain size (104–131 µm; very fine to fine sand; Fig. 8) are consistent with aeolian deposition but do not rule out alluvial deposition. The dominance of subrounded and rounded quartz grains in all except the highest sample, sed_8 (Fig. 9d) and the occurrence of moderate amounts of

https://doi.org/10.1017/qua.2024.36 Published online by Cambridge University Press

Table 3. Luminescence parameters from 125–180 μm quartz and K-feldspar isolates for dating from section 2 of the Ulakhan Sular Formation.[a]

Field code (depth below ground surface and height arl [m])	Lab code	Mineral	Preheat (°C for 10s)	Dose recovery ratio	No. of aliquots (for D_e)	Low dose repeat ratio	High dose repeat ratio	Post-IR OSL ratio	D_0 (Gy)	D_e overdispersion (%)	D_e (Gy)	Total D_r (Gy/ka)	Age (ka)
A17-S2-OSL5 (43.4 m arl; depth: 11.2 m)	GL17115	Quartz	160	1.03 ± 0.03	12	1.03 ± 0.04	1.05 ± 0.03	0.31 ± 0.01	697.7 ± 78.6	14 ± 3	157.9 ± 7.6	2.37 ± 0.09	67 ± 4
		Quartz (H_2SiF_6 treated)			11	0.97 ± 0.05	1.02 ± 0.04	0.97 ± 0.04	81.5 ± 15.9	45 ± 11	303.8 ± 44.2		128 ± 19
		K-feldspar ($pIRIR_{200}$)	-	1.40 ± 0.07	12	0.98 ± 0.03	0.98 ± 0.03	-	317.09 ± 11.8	2 ± 3	341.2 ± 12.8	3.09 ± 0.14	110 ± 7
		K-feldspar ($pIRIR_{250}$)		1.65 ± 0.12		0.99 ± 0.03	0.97 ± 0.03		222.7 ± 10.6	4 ± 4	398.8 ± 17.7		129 ± 8
A17-S2-OSL4 (32.5 m arl; depth: 22.1 m)	GL17114	Quartz	240	0.94 ± 0.07	11	0.90 ± 0.06	0.96 ± 0.05	0.92 ± 0.06	100.4 ± 6.9	27 ± 7	130.8 ± 12.0	1.85 ± 0.08	71 ± 7
		K-feldspar ($pIRIR_{200}$)	-	1.13 ± 0.14	12	0.98 ± 0.03	0.99 ± 0.03	-	243.8 ± 11.0	10.5 ± 3	321.8 ± 16.1	2.92 ± 0.14	110 ± 8
		K-feldspar ($pIRIR_{250}$)		1.42 ± 0.13		1.02 ± 0.06	1.00 ± 0.05		117.6 ± 24.7	38 ± 9	608.1 ± 74.1		208 ± 27
A17-S2-OSL3 (17.1 m arl; 37.5 m depth)	GL17113	Quartz	240	0.96 ± 0.04	12	1.05 ± 0.05	1.06 ± 0.04	0.28 ± 0.02	482.9 ± 48.8	11 ± 2	160.2 ± 6.5	2.19 ± 0.08	73 ± 4
		Quartz (H_2SiF_6 treated)				0.95 ± 0.05	0.98 ± 0.04	0.99 ± 0.05	78.1 ± 17.6	35 ± 8	189.7 ± 4.9		87 ± 4
		K-feldspar ($pIRIR_{200}$)	-	1.16 ± 0.09		0.98 ± 0.03	0.96 ± 0.03	-	323.9 ± 15.2	Zero	378.8 ± 14.2	2.77 ± 0.14	137 ± 8
		K-feldspar ($pIRIR_{250}$)		1.59 ± 0.16		1.01 ± 0.05	0.97 ± 0.05		245.0 ± 18.7		470.8 ± 22.7		170 ± 12
A17-S2-OSL2 (10.8 m arl; 43.8 m depth)	GL17112	Quartz	160	1.07 ± 0.03	12	1.04 ± 0.04	1.01 ± 0.04	0.32 ± 0.01	688.5 ± 85.7	9 ± 2	176.3 ± 6.4	2.32 ± 0.09	76 ± 4
		Quartz (H_2SiF_6 treated)			11	0.98 ± 0.04	0.99 ± 0.04	0.94 ± 0.04	61.7 ± 11.2	35 ± 8	286.8 ± 31.9		124 ± 15
		K-feldspar ($pIRIR_{200}$)	-	1.02 ± 0.10	12	0.97 ± 0.03	0.97 ± 0.03	-	324.3 ± 16.1	10 ± 3	356.0 ± 16.6	3.03 ± 0.14	117 ± 8
		K-feldspar ($pIRIR_{250}$)		1.41 ± 0.15		0.95 ± 0.06	0.97 ± 0.05		230.6 ± 18.9	18 ± 5	374.2 ± 26.3		123 ± 10

A17-S2-OSL1 (6.3 m arl; 48.3 m depth)	GL17111	Quartz	240	0.98 ± 0.04	12	1.08 ± 0.06	1.01 ± 0.04	0.31 ± 0.02	361.0 ± 31.5	13 ± 3	192.5 ± 9.1	1.85 ± 0.08	104 ± 7
		Quartz (H_2SiF_6 treated)				0.94 ± 0.05	1.00 ± 0.04	0.95 ± 0.05	67.4 ± 13.5	31 ± 7	235.7 ± 22.9		128 ± 13
		K-feldspar ($pIRIR_{200}$)	-	1.13 ± 0.08		0.97 ± 0.03	0.97 ± 0.03	-	334.6 ± 16.3	11 ± 3	432.5 ± 21.2	2.55 ± 0.13	170 ± 12
		K-feldspar ($pIRIR_{250}$)		1.24 ± 0.27		1.00 ± 0.05	1.02 ± 0.05		244.0 ± 18.0	42 ± 10	461.6 ± 62.4		181 ± 24

[a]Age estimates expressed relative to 2017. Uncertainties in age are quoted at 1σ confidence, are based on analytical errors, and reflect combined systematic and experimental variability.
Abbreviations: arl, above river level; IR, infrared; OSL, optically stimulated luminescence; pIRIR, post-infrared infrared-stimulated luminescence.

mica (~4–5% biotite and muscovite) in the sediments (Supplementary Table 6) are consistent with limited reworking by wind of alluvial deposits. Although the platy shape of mica crystals facilitates wind transport, mica is relatively soft (Mohs hardness of muscovite 2–2.5) compared to quartz (Mohs 7), and so is rapidly comminuted where it experiences multiple collisions with hard grains during aeolian sand transport, as shown in experiments simulating aeolian and subaqueous abrasion (Anderson et al., 2017). Hence, micas are most likely to persist in the sand fraction of aeolian deposits if in close proximity (no more than tens of kilometers, according to these authors) to their source; but they are expected to become less common if transported much farther, especially in comparison to micas in subaqueously transported sands, where grain-to-grain impacts are less energetic because of the higher viscosity of water than air (Anderson et al., 2017). Finally, sample A17-K-07, beside A17-S2-OSL3 from the Ulakhan Sular Formation, provided only non-identifiable rootlets, consistent with aeolian deposition of these sand-sheet facies.

The only evidence of waterlain deposition of the Ulakhan Sular Formation observed in section 2 was climbing-ripple cross lamination and trough cross lamination present in the basal ~30 cm of the formation (Fig. 5d). Such lamination represents subaqueous current ripples, some of them climbing (e.g., Ashley et al., 1982). Similar climbing-ripple cross lamination is well developed in the Holocene reference example of alluvium (Fig. 4b).

Stratigraphically, the channel-belt deposits in the downstream part of the exposure (sections 1 and 3) are thought to be older than the aeolian deposits in the upstream part (sections 2 and 4) because the latter appear to overlie the former and taper out downstream towards the ground surface (Fig. 3c). In other words, the aeolian deposits of sections 2 and 4 represent a younger aeolian sequence leaning against an older alluvial or fluvio-aeolian terrace (sections 1 and 3).

The fluvial and aeolian sand deposits at Ulakhan Sular have sedimentologic similarities and differences with periglacial fluvio-aeolian and aeolian deposits elsewhere. Analogous modern examples of alluvial sediment supply to wind from both dry riverbeds during summer as well as adjacent sandy geologic formations are provided from Banks Island, western Arctic Canada (Pissart et al., 1977; Good and Bryant, 1985), and the ice-marginal region of western Greenland (Dijkmans and Törnqvist, 1991)—both regions of permafrost and localized fluvio-aeolian sedimentation. Pleistocene sandy deposits of mixed fluvial, aeolian, and fluvio-aeolian origin have been reported from the monsoon regions of China (e.g., Wang et al., 2019; Ding et al., 2023), lowland terrain in northwest Europe (e.g., Vandenberghe and Van Huissteden, 1988; Van Huissteden et al., 2000; Kasse, 2002; Schokker and Koster, 2004; Kasse et al., 2007; Worsley, 2015), and western Arctic Canada (Murton and Bateman, 2007, fig. 2b). What is different, however, is that the Ulakhan Sular aeolian deposits we examined did not alternate with fluvial deposits, as is common in the sequences referred to above, but represent aeolian reworking of them in one or more major episodes. In terms of depositional environments, the sequence at Ulakhan Sular is considered an aeolian-influenced fluvial system, with similarities to that at Epiguruk on the Kobuk River of northwest Alaska (Ashley and Hamilton, 1993). However, our reconnaissance study did not identify floodplain deposits similar to those at Epiguruk, and further investigation is warranted. What is remarkable about the Ulakhan Sular sand-sheet deposits is their great

https://doi.org/10.1017/qua.2024.36 Published online by Cambridge University Press

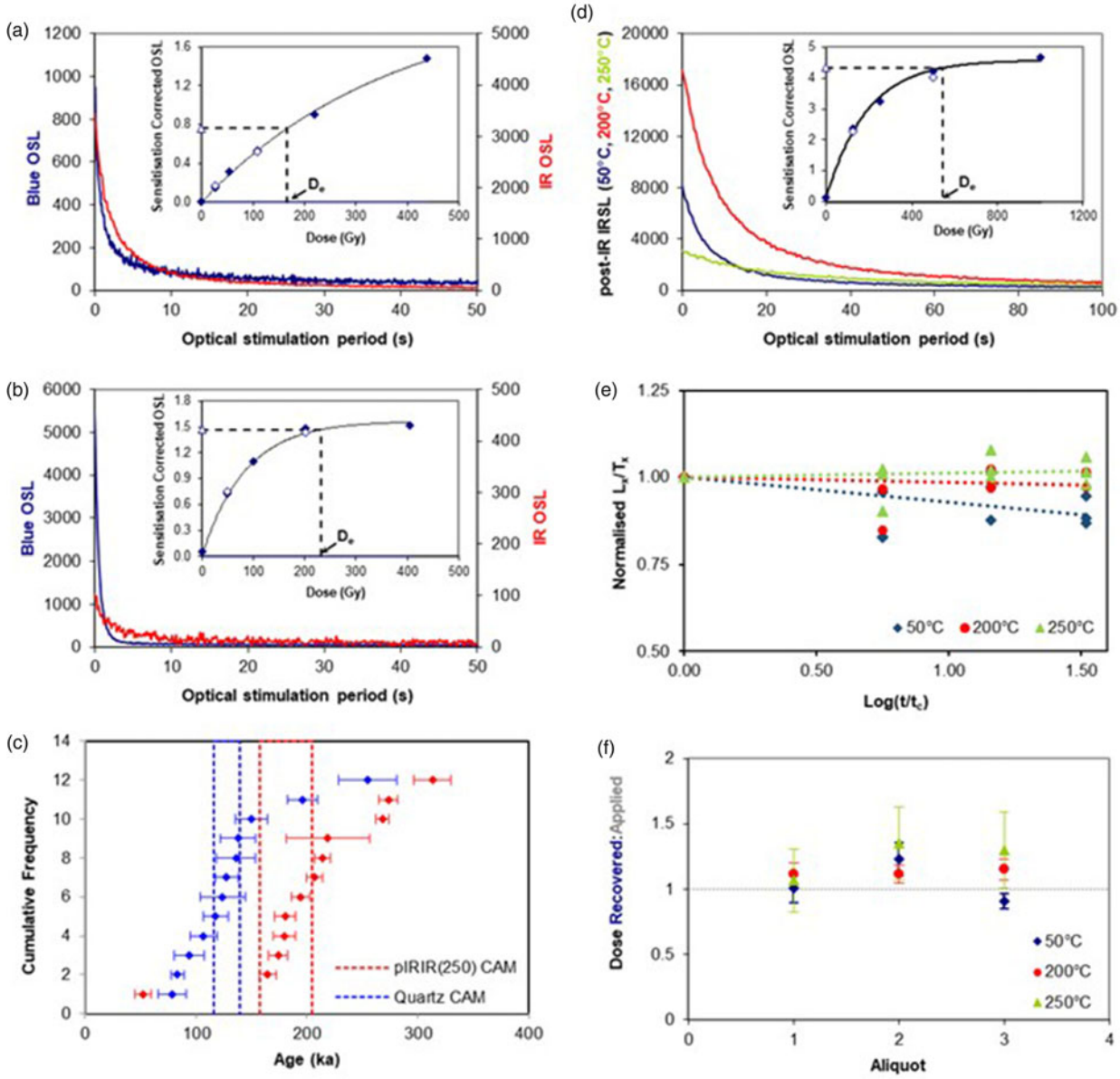

Figure 13. Example luminescence data for GL17111; (a and b) Dose-response curves (DRCs; open triangle, natural signal; closed diamonds, regenerative-dose signals; open diamonds, repeat regenerative doses), blue optically stimulated luminescence (OSL) and infrared-stimulated luminescence (IRSL) decay of quartz aliquots (a) pre- and (b) post-H_2SiF_6. (c) Quartz OSL and K-feldspar $pIRIR_{250}$ age distributions. (d) K-feldspar $pIRIR_{250}$ DRC and IR_{50}, $pIRIR_{200}$, and $pIRIR_{250}$ signal decay. (e) Signal depletion as a function of storage time for the IR_{50} (blue diamonds), $pIRIR_{200}$ (red circles), and $pIRIR_{250}$ (green triangles): storage times (t) and L_x/T_x ratios were normalized to the first/prompt measurements (t_c) at 62 h. (f) Dose recovery ratios for IR_{50}, $pIRIR_{200}$, and $pIRIR_{250}$ of three aliquots.

thickness (~50 m). Such thickness may reflect an abundance of local sand sources, ample accommodation space in the Nizhneadychanska depression, and intensive aeolian transport and deposition. To our knowledge, this is the thickest sequence of aeolian sand-sheet deposits reported anywhere from present or past periglacial regions, though detailed sedimentologic examination of high sandy bluffs elsewhere in Siberia (for example at Mamontova Gora, on the lower course of the River Aldan; Fig. 1a; Vangengeim, 1961, pp. 20–25) might identify other thick aeolian deposits. Fluvial deposits with thicknesses >50 m are not unusual.

Sand sources

The Ulakhan Sular Formation occurs on the eastern margins of the Nizhneadychanska and Verkhoyansk depressions (Fig. 2). Sand sources likely comprised the paleochannels of the rivers Adycha and Yana, as well as Pliocene-aged sand and fine sand of the adjacent Tabalakh Formation, and the sandy deposits of the Ust-Nelgehinski Formation (Fig. 2). Based on the geographic and stratigraphic distribution of the Ulakhan Sular Formation (Fig. 2), it is likely that some of the sand was banked up against the margins of both depressions and/or that the rivers Adycha and Yana have eroded away a substantial amount of the formation in the central parts of the depressions. The heavy mineral data from the aeolian sand-sheet deposits of the Ulakhan Sular Formation (Supplementary Table 7), however, are distinctly different from those of the alluvial Ust-Nelgehinski Formation, which is dominated by limonite (Supplementary text 1). More similarities are noted with heavy minerals in the alluvial

https://doi.org/10.1017/qua.2024.36 Published online by Cambridge University Press

Table 4. Radiocarbon ages of organic remains from section 2 of the Ulakhan Sular Formation and from the bank of the Adycha River at the Holocene alluvium reference site

Sample ID	Depth (m below ground surface)	Lab ID	$F^{14}C$	^{14}C age (^{14}C yr BP)	Calibrated age range (2σ) (cal yr BP)	Calibrated median age (cal yr BP)	Dated material	Host material
A17-S2-AMS7	11.2	Poz-102531		>47,000	n.a.	n.a.	In situ roots and rhizomes	Aeolian sand sheet (HAB)[a]
A17-S2-AMS6	22.1	Poz-102530		43,000 ± 2000	49,560–42,607	45,762	In situ roots	Aeolian sand sheet (HAB)
A17-K-03	2.0	AWI1687.1.1	0.9738 ± 0.0132	213 ± 109	458–0	217	Rootlets and *Larix* needle	Modern riverbank

[a]HAB, horizontal alternating bedding.

Adycha Formation, which underlies the Ulakhan Sular Formation (e.g., the presence of ilmenite, garnet, amphibole, pyroxene, and tourmaline). Some mineralogical differences between the aeolian sand-sheet deposits and potential alluvial sources are to be expected in view of different sediment transport conditions.

Forest bed

The woody peat lens in section 1 is interpreted as a forest bed infill of a gully or local channel. The lower contact of the lens, which is concave-up and has a relief of 2–3 m, indicates the maximum depth of incision. The infill contains abundant woody remains. Its characteristics resemble those of discontinuous bodies of woody material interpreted as a forest bed above an erosional surface (i.e., disconformity) in the top of the lower sand unit at Batagay megaslump (Murton et al., 2017, 2022). Kaplina et al. (1983) observed a similar lens of wood-enriched peat in a similar stratigraphic position at Ulakhan Sular, interpreting it as a small trough rapidly infilled with sediment and vegetation that grew nearby. Lastly, the buried soil interbed below the lower level of ice wedges near the top of the Ulakhan Sular Formation (Fig. 6f) within underlying sands has ferruginous spots and streaks that indicate freezing under open conditions.

Thermal contraction cracking and substrate stability

Wedges formed by infilling of thermal contraction cracks in the Ulakhan Sular Formation indicate changing conditions of substrate stability and deposition during their development. Tall and narrow, syngenetic, composite sand–ice wedges and sand wedges of primary infilling closely resemble chimney-like sand wedges within aeolian sand-sheet deposits of the Kittigazuit Formation, Northwest Territories, Canada (Murton and Bateman, 2007) and indicate formation in dry conditions (i.e., not enough snowmelt water to form ice wedges) and/or rapid aggradation of sand. Kaplina et al. (1983) identified two horizons of similar syngenetic structures but termed them "soil wedges" and connected their formation with the infilling of the cracks by thawed soil within an active layer. The strongly depleted $\delta^{18}O$ values of composite wedges point to their formation in a cold climate, i.e., glacial times (compare Porter and Opel, 2020). However, the contrasting δD and *d* values indicate substantial secondary fractionation processes that do not allow a conclusive interpretation.

Epigenetic ice wedges were observed in and adjacent to the woody lens in section 1, in two stratigraphic levels (i.e., generations) near the top of the Ulakhan Sular Formation (Fig. 6f), and also beneath a thermoerosional gully in the upper part of it (Fig. 7). The ice wedges suggest one or more periods of surface stability, with little or no sand aggradation and sufficient snowmelt water to form ice wedges. The ice wedges all remain to be dated, though, the lower level in Figure 6f is potentially of Kargin (MIS 3) or Sartanian (MIS 2) age. Of these, the former is more likely as ice wedges of MIS 2 age have rarely been observed in northeast Siberia, either because they have been eroded during late-glacial–Holocene warming or because they formed only in specific settings (e.g., valleys; see Wetterich et al., 2011, 2021 for Bol'shoy Lyakhovsky Island). The upper level of ice wedges together with the ice wedge in Figure 7 are potentially of Holocene age.

Holocene deposits

The uppermost ~2 m of the sedimentary sequence at section 2, resting directly on top of the Ulakhan Sular Formation, are interpreted as deposits of a pond or small lake, based on the mollusc remains, horizontal parallel stratification, and abundant interbedded organic remains (Supplementary Table 2, Fig. 7). Macrofossil sample A17-K-05 (1.7 m bgs) is from a sedimentary layer presumably of Holocene age and stratigraphically beneath the mollusc-bearing horizon (A17-S2-Sed8). The macrofossil assemblage suggests the former presence of *L. gmelinii* woodlands, with birch, *Betula* sp., and raspberry, *Rubus idaeus,* in the understory layer, and blunt leaf sandwort, *Moehringia lateriflora,* and sedges, Cyperaceae, in forest clearings. At the same time, a prominent amount of pondweed, *Potamogeton* spp., fruits, and *Daphnia* eggs points to the presence of small lakes or ponds with goosefoot, *Chenopodium*, growing along their margin. Several well-preserved elytra were found in the sample: from harp ground beetles *Pterostichus* (*Cryobius*) *ventricosus* Esch. and *Pterostichus* (*Lenapterus*) *vermiculosus* Men.; ground beetles *Dicheirotrichus mannerheimii* Sahlb.; and a true weevil *Ceutorhynchus* sp. Identified harp ground beetle species usually occupy wet environments and can be found in woodlands along waterbodies and under mosses (Reyes et al., 2010), which is consistent with the plant macrofossil finds of aquatic and subaquatic taxa. The ground beetle *Dicheirotrichus mannerheimii* Sahlb. and true weevil *Ceutorhynchus*, unlike harp beetles, inhabit well-drained sites and woodlands (Sher and Kuzmina, 2013; Korotyaev, 2020), which is in line with macrofossils characteristic of woodland vegetation. Although *Ceutorhynchus* taxa feed on Brassicaceae and Asteraceae (Korotyaev, 2020), the remains of these plants are missing in the plant macrofossil assemblage. The studied plant macrofossil sample supports the sedimentologic

https://doi.org/10.1017/qua.2024.36 Published online by Cambridge University Press

interpretation (Supplementary Table 2) that this horizon accumulated within ponds and small lakes, and expands the paleoecological reconstruction by providing evidence for woodland vegetation. Kaplina et al. (1983) also observed mollusc remains within these deposits and attributed the deposits to a channel and riverbank. Pond deposits similar to those we identify at Ulakhan Sular have been reported from floodplain deposits of the Kobuk River, at Epiguruk, northwest Alaska (Ashley and Hamilton, 1993).

The Holocene alluvium reference site ~3 km upstream of the Ulakhan Sular exposures provided a sample (A17-K-03) from a depth of 2 m bgs which included several *L. gmelinii* needles, *Betula* sp., and Cyperaceae nutlets, as well as moss remains. Collectively, these remains suggest an open woodland environment without the direct presence of aquatic taxa. The stable isotope composition of ice wedge A17-IW3 sampled at this site reflects the Late Holocene to modern, continental cold winter climate conditions (see Opel et al., 2019 for more discussion).

Age

Because the calibrated median age of 45,760 cal yr BP from in situ roots (Poz-102530) is near the limit of radiocarbon dating and is probably a minimum age for sand deposition, we consider the luminescence ages alone. Arising from differing luminescence signals and dose rates, the statistical concordance between post-H_2SiF_6 quartz OSL and both $pIRIR_{200}$ and $pIRIR_{250}$ K-feldspar age estimates for samples GL17112 and GL17115 is likely the strongest index of reliability in luminescence dating at Ulakhan Sular. Given these samples' stratigraphic positions and their associated 1σ uncertainty in age giving an age range of 147–103 ka, they suggest the aeolian sediment sequence largely formed during late MIS 6 to MIS 5. Beyond these two samples, the pIRIR K-feldspar age estimates are significantly older than their quartz OSL counterparts and, for samples GL17113 and GL17114, the $pIRIR_{250}$ ages are older than those derived from $pIRIR_{200}$. This pattern likely stems from differential bleaching prior to burial, rooted in the relatively lower bleaching rates of K-feldspar relative to quartz, and of $pIRIR_{250}$ relative to $pIRIR_{200}$, leading to age overestimation by K-feldspar. The reduction in IR signal, improvement in post-IR OSL ratio, and increase in age for quartz after H_2SiF_6 digestion suggest this treatment is effective in removing contamination by an IR-bearing mineral. The post-H_2SiF_6 quartz OSL age estimates are, therefore, likely the more reliable luminescence chronometer at Ulakhan Sular. A late MIS 6 to MIS 5 age for the Ulakhan Sular Formation is stratigraphically consistent with older electron spin resonance ages from the underlying Adycha Formation. Ages of 360 ± 17 ka and 212 ± 10 ka were obtained by Nikolskiy (2010) from bivalve shells at Ulakhan Sular. These suggest deposition during MIS 11–10 and, according to P.A. Nikolskiy (personal communication, 2019), MIS 7–6, respectively.

Kaplina et al. (1983) obtained a radiocarbon age of ≥43,000 years ago (MSU-570) from a layer of woody peat that we believe is at the same stratigraphic level as the lens of woody peat we observed in section 1 (Fig. 3). This age refutes the assumption of A.I. Tomskaya (Tomskaya and Savvinova, 1971) that a significant thickness of the underlying sandy sequence accumulated during the Karginsky interstadial period (~MIS 3). Instead, we tentatively assign the woody peat to the last interglacial period (MIS 5e) based on the occurrence of tree remains assumed to originate from taiga vegetation. Before the Holocene, MIS 5e was the most recent period with a known occurrence of taiga forests in this region (Ashastina et al., 2018).

Overall, the likely age of late MIS 6 to MIS 5 for deposition of the Ulakhan Sular Formation supports the suggestions by Sher et al. (2011) that the formation dates to the latest Middle Pleistocene to early Late Pleistocene, and also by Kaplina et al. (1983) that the bulk of the sequence at Ulakhan Sular is of Middle Pleistocene age, possibly with Late Pleistocene age deposits at the top.

Regional correlations and paleoenvironmental significance

The aeolian sand-sheet deposits of the Ulakhan Sular Formation can be correlated with other MIS 6–5e deposits in western and eastern Beringia, southern Siberia, and in marine sediment cores in the North Pacific Ocean.

Within the Batagay–Betenkes study area (Fig. 2), we correlate the sand-sheet deposits with the lower sand unit of the Batagay megaslump. Both units comprise aeolian sand-sheet deposits; contain narrow, chimney-like sand wedges or composite wedges; appear to be beyond the range of ^{14}C dating (i.e., before MIS 3); and provide luminescence ages that overlap in MIS 6. The lower sand unit at Batagay has provided a quartz OSL age of 142.8 ± 25.3 ka and a feldspar IRSL age of 210.0 ± 23.0 ka, in addition to minimum quartz OSL ages of >93.6 ka, >95.2 ka, >100.2 ka, and >123.2 ka (Ashastina et al., 2017), ages that have been attributed to MIS 6 or older (Murton et al., 2023). Lastly, the irregular base of the woody lens in section 1 at Ulakhan Sular (Table 1) represents an erosional event cutting into the underlying sediments, similar to the erosional surface (disconformity), locally gullied, beneath the upper forest bed of likely MIS 5e age at Batagay (Murton et al., 2017, 2022). Wood fragments (i.e., from trees) in this region are mainly limited to interglacial periods, and hence the woody lens at Ulakhan Sular likely also represents the same interglacial period that followed deposition of sand sheets at both sites.

Beyond the study area but within the adjacent Yana–Indigirka Lowland, a correlation is drawn with the Kuchchugui Suite at Oyogos Yar, along the southern coast of Dmitry Laptev Strait (Fig. 1a). The Kuchchugui Suite also occurs on the northern coast of Dmitry Laptev Strait, along the southern part of Bol'shoy (Great) Lyakhovsky Island. The suite comprises syncryogenic, ice-poor sandy and silty deposits—horizontally laminated and containing numerous grass roots and small (≤10 cm) peat inclusions (Wetterich et al., 2016; Tumskoy and Kuznetsova, 2022)—attributed to alluvial floodplain deposition with shallow lakes (Andreev et al., 2004; Opel et al., 2017) or distal glaciofluvial deposition related to the deglaciation of the East Siberian Ice Sheet (Tumskoy, 2012). Syngenetic ice wedges and composite sand–ice wedges within the Kuchchugui Suite were reported by Opel et al. (2017), together with an IRSL age of 112.5 ± 9.6 ka from near the top of it and attributed to early MIS 5. Stratigraphically, the Kuchchugui Suite underlies the Bychchagy Ice Complex, dated by $^{230}Th/U$ of peaty horizons to between 126 +16/−13 ka and 89 ± 5 ka (i.e., MIS 5e–5b) (Wetterich et al., 2016, 2019), and so the Kuchchugui Suite is likely of MIS 6 age. The syngenetic composite wedges at both Ulakhan Sular and Oyogos Yar suggest a component of aeolian sand infilling of thermal contraction cracks. Abundant non-identifiable arboreal pollen (reworked Pinaceae) and low pollen concentrations (mostly Poaceae and Cyperaceae) in Kuchchugui Suite sediments have been interpreted as evidence of sparse

https://doi.org/10.1017/qua.2024.36 Published online by Cambridge University Press

grass–sedge vegetation and an extremely cold climate at the end of the Middle Pleistocene (Andreev et al., 2004; Wetterich et al., 2016). Such conditions are consistent with glaciation nearby.

Glaciation by the East Siberian Ice Sheet is thought to have centered on the uplands of Zhokhov and Bennett islands in the De Long Archipelago, from which ice hundreds of meters thick radiated outwards over an area of ~150,000–200,000 km^2 of the emergent East Siberian Shelf (Fig. 1a) (Tumskoy, 2012). The ice glaciotectonically deformed permafrost on New Siberia Island (Golionko et al., 2019). The limits of glaciation are uncertain, though the southern limit was probably located in the Sannikov Strait, which separates the Lyakovsky Islands in the south from the Anzhu Islands in the north (Basilyan et al., 2008). Glaciation probably took place during MIS 6 (~190–132 ka; Brigham-Grette, 2013; Niessen et al., 2013), as determined from uranium–thorium dating of marine mollusc shells in glaciotectonically deformed permafrost together with biostratigraphic constraints obtained from the remains of pre-glacial lemmings (Nikolskiy et al., 2017).

Farther east in western Beringia, sedimentary records from Lake El'gygytgyn, central Chukotka (Fig. 1a), indicate that regional climate varied from cold and dry (MIS 6.4 and 6.2), to cold and moist (MIS 6.6; cf. Zhao et al., 2022), to warm (MIS 6.5, 6.3, and 6.1) (Melles et al., 2007). Intense aridity during cold and dry climate conditions of MIS 6.4 and 6.2 has been attributed to predominantly westerly winds (Melles et al., 2007), with northeast Siberia effectively in the rain shadow of an ice sheet in northern Eurasia. These authors suggested that moister conditions of the cold and moist climate mode during MIS 6.6 resulted from northerly or easterly winds reaching northeast Siberia more frequently because the Siberian High (anticyclone) migrated westward or weakened. The vegetation near Lake El'gygytyn during MIS 6 was that of a cold steppe (Wennrich et al., 2016), being herb-dominated, sparse, and the landscape largely barren (Lozhkin et al., 2007). The lake level was low (Fedorov et al., 2019). Evidence of aeolian sediment transport onto the surface of lake ice during cold and dry conditions is provided by sediment clasts formed by agglomeration of windblown particles during transport and descent through vertical conduits in perennial ice cover and onto the lake bed (Melles et al., 2007), similar to windblown sand accumulating on and penetrating through the perennial ice cover of modern Lake Hoare, Antarctica (Squyres et al., 1991).

In central Yakutia, weathered aeolian deposits of sandy silt (loess) of MIS 6 age occur on a terrace of the Tumara River (Fig. 1a; e.g., Zech et al., 2008). Another correlation of the Ulakhan Sular sand-sheet deposits is potentially with the lower (gray) silt unit of Péwé et al. (1977) at Mamontova Gora, beside the Aldan River (Fig. 1a). T.L. Péwé interpreted the lower silt as loess. Its age, however, is uncertain. Péwé et al. (1977) suggested it accumulated during the Samarov glaciation, which is equated with MIS 8 (Astakhov et al., 2016). An alternative age of MIS 6 is also feasible, based on a U/Th age of 176 ± 2 ka BP (Katasonov and Ivanov, 1973) from "lacustrine loamy deposits" above alluvial deposits at Mamontova Gora (Cherbunina et al., 2021). New OSL ages for this unit (138 ± 15 and 126 ± 11 ka; Torgovkin et al., 2024) rather indicate a late MIS 6 to early MIS 5 age. Further systematic dating of the sequence is needed. Péwé et al. (1977) concluded that the lower silt closely resembled the Gold Hill Loess near Fairbanks, central Alaska, whose age ranges from ~3 Ma to 130 ka (Péwé et al., 2009). Recent dating of the Old Crow tephra—which is common within loess sequences at multiple sites in central Alaska (e.g., Jensen et al., 2013; Bigelow et al., 2014)—to 159 ± 8 ka (Reyes et al., 2023), confirms significant loess deposition during MIS 6 (Jensen et al., 2016). Likewise, loess of MIS 6 age occurs at multiple sites in southern Siberia (Chlachula, 2003).

Collectively, the correlations proposed above suggest that aeolian deposition of cold-climate sand and silt (loess) was common in areas of both western and eastern Beringia and south into southern Siberia during part of MIS 6. This is consistent with higher dust fluxes and mass accumulation rates (MARs) of aeolian deposits in the central Chinese Loess Plateau (CLP) during glacial periods relative to interglacial intervals (Nugteren and Vandenberghe, 2004; Sun and An, 2005), though the glacial–interglacial differences decreased in the southern part of the CLP. Similarly, higher dust fluxes are recorded in some western North Pacific sediment cores from the glacial period MIS 6 compared to the previous and subsequent interglacial periods (Abell et al., 2023; Zhong et al., 2024). In the central CLP, mean MARs and the mean grain size of quartz during MIS 6 were higher in its final stadial (i.e., MIS 6a/6.6) than in earlier times of MIS 6 and also higher than in the last glacial maximum (LGM). This was interpreted as indicating that interior Asia was more arid and subject to stronger paleowinds later in the penultimate glaciation compared with the LGM (Sun and An, 2005). Regionally across the CLP, dust fluxes tended to be higher during the last part of MIS 6 (a "superglacial"/extreme glacial) than at any other time during the last 250 ka, including the LGM (Nugteren and Vandenberghe, 2004). This late MIS 6 episode of enhanced aeolian deposition is consistent with a late MIS 6 age for aeolian sand at Ulakhan Sular. More generally, enhanced aeolian deposition is expected during glacial climates of the late Quaternary when meridional temperature gradients became steeper and therefore increased the intensity and frequency of high-speed wind events in dust source areas (McGee et al., 2010). By the same reasoning, sandy source areas in some high-latitude, sandy braided-river deposits such as at Ulakhan Sular would also have been subject to aeolian reworking and deposition during glacial climates, as occurred regionally in northwest North America and northern Eurasia during the glacial climate of MIS 2 (Murton et al., 2015, see figs. 31 and 32 therein).

Limitations and future research

The detailed stratigraphy between the various sedimentary deposits identified along the 2-km-long outcrop at Ulakhan Sular needs documenting carefully (cf. Hamilton and Ashley, 1993) to clarify the stratigraphic relationships between the aeolian sand-sheet deposits in sections 2 and 4 and the fluvial deposits in sections 1 and 3. Likewise detailed examination of the upper meters of the Ulakhan Sular Formation is needed to differentiate it from overlying deposits of likely Holocene age. Systematic luminescence dating of the Ulakhan Sular Formation is needed to confirm the late MIS 6 to MIS 5 age and to test the hypothesis that deposition of the sand sheet was rapid. Dating is also needed to determine the age relationships between the woody peat lens in section 1 and the multiple layers of organic material observed in 2023 south of section 2, as well as establishing the ages of the ice wedges. Additional heavy mineral analysis of a variety of Miocene, Neogene, and Pleistocene sandy units would help to identify the sand sources for both the Adycha and Ulakhan Sular formations.

Conclusions

Several conclusions arise from this study. Sedimentologically, the Ulakhan Sular Formation at the stratotype section contains

https://doi.org/10.1017/qua.2024.36 Published online by Cambridge University Press

channel-belt deposits of a sandy braided river replaced upriver by younger, aeolian sand-sheet deposits. The formation also contains ice wedges, sand wedges, and composite wedges. It is capped by the organic-rich deposits of a small pond or lake. Overall, it is interpreted as a fluvio-aeolian unit deposited in a permafrost environment.

The fluvio-aeolian deposits at Ulakhan Sular have sedimentologic similarities and differences with periglacial fluvio-aeolian and aeolian deposits in modern arctic regions of Canada and Greenland, and Pleistocene deposits in Alaska, China, and northwest Europe. Unusually, the aeolian sand-sheet deposits at Ulakhan Sular are remarkably thick (~50 m), likely because of abundant local sand sources, ample accommodation space, and intensive aeolian transport and deposition. Additionally, the aeolian deposits at Ulakhan Sular do not alternate with fluvial deposits but represent reworking of them in one or more major episodes.

An age of MIS 6/5 for aeolian sand-sheet deposition at Ulakhan Sular is likely, based on the coeval estimates from post-H_2SiF_6 quartz OSL, and $pIRIR_{200}$ and $pIRIR_{250}$ on K-feldspar in samples GL17112 and GL17115. Based on 1σ uncertainties in age associated with these signals and samples, their age range (147–103 ka) suggests relatively rapid deposition of the aeolian sand, which is consistent with the narrow, chimney-like form of the permafrost wedges within it.

The aeolian genesis and rapid accumulation of part of the Ulakhan Sular Formation is consistent with other data on the widespread, previously underestimated participation of aeolian sediments in the structure of large river valleys both in central Siberia (e.g., Galanin, 2021; Lukyanycheva et al., 2024) and in European Russia (e.g., Zaretskaya et al., 2024).

The aeolian sand-sheet deposits of the Ulakhan Sular Formation are correlated with other cold-climate aeolian sand and silt deposits and associated stratigraphic units of probable MIS 6 age at the nearby Batagay megaslump, several sites in western and eastern Beringia, and in southern Siberia.

This correlation indicates a regional episode of strengthened aeolian sand and dust transport and deposition during late MIS 6 in Beringia and southern Siberia at a similar time to glaciation by the East Siberian Ice Sheet on the emergent East Siberian Shelf.

Supplementary material. The supplementary material for this article can be found at https://doi.org/10.1017/qua.2024.36

Acknowledgments. Senior editor Derek Booth, associate editor Tom Lowell, and reviewers Andrei Panin and Jef Vandenberghe are thanked for their valuable comments on earlier drafts. This research has been supported by the Deutsche Forschungsgemeinschaft (grant nos. OP217/3-1, OP217/4-1), the Leverhulme Trust (Research Project Grant RPG-2020-334), Russian Science Foundation (grant project 23-27-00242), and by the Royal Society (grant no. IE150192 to Mary Edwards, University of Southampton). Aleksei Lupachev and Yana Tikhonravova's 2023 field expedition, pedological and cryolithological studies, and further analytical data processing were supported by the Russian Science Foundation, grant project 23-27-00242 (https://rscf.ru/en/project/23-27-00242/). We thank the AWI Sedimentology Lab for carrying out the sediment analyses and the AWI ISOLAB FACILITY, i.e., Hanno Meyer and Mikaela Weiner, for stable isotope analysis. Katarzyna Piper is thanked for copyediting of the manuscript.

References

Abell, J.T., Winckler, G., Pullen, A., Kinsley, C.W., Kapp, P.A., Middleton, J.L., Pavia, F.J., McGee, D., Ford, H.L., Raymo, M.E., 2023. Evaluating the drivers of Quaternary dust fluxes to the western North Pacific: East Asian dustiness and Northern Hemisphere gustiness. *Paleoceanography and Paleoclimatology* **38**, e2022PA004571. https://doi.org/10.1029/2022PA004571

Anderson, C.J., Struble, A., Whitmore, J.H., 2017. Abrasion resistance of muscovite in aeolian and subaqueous transport experiments. *Aeolian Research* **24**, 33–37.

Andreev, A.A., Grosse, G., Schirrmeister, L., Kuzmina, S.A., Novenko, E.Y., Bobrov, A.A., Tarasov, P.E., *et al.*, 2004. Late Saalian and Eemian palaeoenvironmental history of the Bol'shoy Lyakhovsky Island (Laptev Sea region, Arctic Siberia). *Boreas* **33**, 319–348.

Ashastina, K., Kuzmina, S., Rudaya, N., Troeva, E., Schoch, W.H., Römermann, C., Reinecke, J., *et al.*, 2018. Woodlands and steppes: Pleistocene vegetation in Yakutia's most continental part recorded in the Batagay permafrost sequence. *Quaternary Science Reviews* **196**, 38–61.

Ashastina, K., Schirrmeister, L., Fuchs, M., Kienast, F., 2017. Palaeoclimate characteristics in interior Siberia of MIS 6–2: first insights from the Batagay permafrost mega-thaw slump in the Yana Highlands. *Climate of the Past* **13**, 795–818.

Ashley, G.M., Hamilton, T.D., 1993. Fluvial response to late Quaternary climatic fluctuations, central Kobuk Valley, northwestern Alaska. *Journal of Sedimentary Petrology* **63**, 814–827.

Ashley, G.M., Southard, J.B., Boothroyd, J.C., 1982. Deposition of climbing-ripple beds: a flume simulation. *Sedimentology* **29**, 67–79.

Ashworth, P.J., Sambrook Smith, G.H., Best, J.L., Bridge, J.S., Lane, S.N., Lunt, I.A., Reesink, A.J.H., Simpson, C.J., Thomas, R.E., 2011. Evolution and sedimentology of a channel fill in the sandy braided South Saskatchewan River and its comparison to the deposits of an adjacent compound bar. *Sedimentology* **58**, 1860–1883.

Astakhov, V., 2014. The postglacial Pleistocene of the northern Russian mainland. *Quaternary Science Reviews* **92**, 388–408.

Astakhov, V., Shkatova, V., Zastrozhnov, A., Chuyko, M., 2016. Glaciomorphological map of the Russian Federation. *Quaternary International* **420**, 4–14. https://doi.org/10.1016/j.quaint.2015.09.024

Basilyan, A.E., Nikol'skii, P.A., Anisimov, M.A., 2008. Pleistocene glaciation of the New Siberian Islands—no more doubts. [In Russian.] *Novosti MPG* 2007/2008 **12**, 7–9.

Bateman, M.D., 2008. Luminescence dating of periglacial sediments and structures. *Boreas* **37**, 574–588.

Bateman, M.D., Murton, J.B., 2006. Late Pleistocene glacial and periglacial aeolian activity in the Tuktoyaktuk Coastlands, NWT, Canada. *Quaternary Science Reviews* **25**, 2552–2568.

Bigelow, N., Edwards, M.E., Elias, S.A., Hamilton, T.D., Schweger, C.E., 2014. Tundra and boreal forest of interior Alaska during terminal MIS 6 and MIS 5e. *Vegetation History and Archaeobotany* **23**, 177–193.

Blodgett, K.H., Stanley, K.O., 1980. Stratification, bedforms and discharge relations of the braided Platte River system, Nebraska. *Journal of Sedimentary Petrology* **50**, 139–148.

Brigham-Grette, J., 2013. A fresh look at Arctic ice sheets. *Nature Geoscience* **6**, 807–808.

Cant, D.J., Walker, R.G., 1978. Fluvial processes and facies sequences in the sandy braided South Saskatchewan River, Canada. *Sedimentology* **25**, 625–648.

Carter, D.L., 1981. A Pleistocene sand sea on the Alaskan Arctic Coastal Plain. *Science* **211**, 381–383.

Cherbunina, M.Y., Karaevskaya, E.S., Vasil'chuk, Y.K., Tananaev, N.I., Shmelev, D.G., Budantseva, N.A., Merkel, A.Y., *et al.*, 2021. Microbial and geochemical evidence of permafrost formation at Mamontova Gora and Syrdakh, central Yakutia. *Frontiers in Earth Science* **9**, 739365. https://doi:10.3389/feart.2021.739365

Chlachula, J., 2003. The Siberian loess record and its significance for reconstruction of Pleistocene climate change in north-central Asia. *Quaternary Science Reviews* **22**, 1879–1906.

Collinson, J.D., 1970. Bedforms of the Tana River, Norway. *Geografiska Annaler Series A* **52**, 31–56.

Collinson, J., Mountney, J., Thompson, N., 2006. *Sedimentary Structures*. 3rd ed. Academic Press, Dunedin.

Dallimore, S.R., Wolfe, S.A., Matthews, J.V., Jr., Vincent, J.-S., 1997. Mid-Wisconsinan eolian deposits of the Kittigazuit Formation, Tuktoyaktuk Coastlands, Northwest Territories, Canada. *Canadian Journal of Earth Sciences* **34**, 1421–1441.

Dansgaard, W., 1964. Stable isotopes in precipitation. *Tellus* **16**, 436–468.

Dijkmans, J.W.A., Törnqvist, T.E., 1991. *Modern Periglacial Eolian Deposits and Landforms in the Søndre Strømfjord Area, West Greenland and their Palaeoenvironmental Implications*. Meddelelser Om Grønland, Geoscience 25. The Commission for Scientific Research in Greenland, Copenhagen.

Ding, Z., Lu, R., Liu, X., Chen, D., 2023. High-northern-latitude forcing modulated fluvial–aeolian interplay during the Last Glacial Period in the Mu Us Desert, northern central China. *Quaternary Science Reviews* **315**, 108255. https://doi.org/10.1016/j.quascirev.2023.108255

Fedorov, G., Andreev, A.A., Raschke, E., Wennrich, V., Schwamborn, G., Glushkova, O.Y., Juschus, O., Zander, A., Melles, M., 2019. Middle to Late Pleistocene lake-level fluctuations of Lake El'gygytgyn, far-east Russian Arctic. *Boreas* **48**, 516–533.

Galanin, A.A., 2021. Late Quaternary sand covers of central Yakutia (eastern Siberia): structure, facies composition and paleoenvironment significance. *[In Russian.] Kriosfera Zemli* [Earth's Cryosphere] **25**, 3–30.

Germonpré, M., Fedorov, S., Danilov, P., Galeta, P., Jimenez, E-L., Sablin, M., Losey, R.J., 2017. Palaeolithic and prehistoric dogs and Pleistocene wolves from Yakutia: identification of isolated skulls. *Journal of Archaeological Science* **78**, 1–19.

Glushkova, O. Yu., 2011. Late Pleistocene glaciations in North-East Asia. In: Ehlers, J., Gibbard, P.L., Hughes, P.D. (Eds.), *Quaternary Glaciations – Extent and Chronology: A Closer Look*. Developments in Quaternary Science 15. Elsevier, Amsterdam, pp. 865–875.

Golionko, B.G., Basilyan, A.E., Nikolsky, P.A., Kostyleva, V.V., Malyshev, N.A., Verzhbitsky, V.E., Obmetko, V.V., Borodulin, A.A., 2019. Fold–thrust deformations of New Siberia Island (Novosibirsky Islands, Russia): age, morphology, and genesis of structures. *Geotectonics* **53**, 675–699.

Good, T.R., Bryant, I.D., 1985. Fluvio–aeolian sedimentation – an example from Banks Island, N.W.T., Canada. *Geografiska Annaler* **67A**, 33–46.

Grigoriev, S.E., Cheprasov, M. Yu., Savvinov, G.N., Tikhonov, A.N., Novgorodov, G.P., Fedorov, S.E., Boeskorov, G.G., *et al.*, 2017. Paleontological and archaeozoological researches in the Yana River Basin. [In Russian.] *Vestnik of North-Eastern Federal University* **57**, 20–35.

Hamilton, T.D., Ashley, G.M., 1993. Epiguruk: a late Quaternary environmental record from northwestern Alaska. *Geological Society of America Bulletin* **105**, 583–602.

Hopkins, D.M., 1982. Aspects of the paleogeography of Beringia during the late Pleistocene. In: Hopkins, D.M., Matthews, J.V., Jr., Schweger, C.E., Young, S.B. (Eds.), *Paleoecology of Beringia*. Academic Press, New York, pp. 3–28.

IUSS Working Group WRB, 2022. *World Reference Base for Soil Resources. International Soil Classification System for Naming Soils and Creating Legends for Soil Maps*. 4th ed. International Union of Soil Sciences (IUSS), Vienna, Austria.

Jensen, B.J.L., Evans, M.E., Froese, D.G., Kravchinsky, V.A., 2016. 150,000 years of loess accumulation in central Alaska. *Quaternary Science Reviews* **135**, 1–23.

Jensen, B.J.L., Reyes, A.V., Froese, D.G., Stone, D.B., 2013. The Palisades is a key reference site for the middle Pleistocene of eastern Beringia: new evidence from paleomagnetics and regional tephrostratigraphy. *Quaternary Science Reviews* **63**, 91–108.

Kaplina, T.N., Kartashova, G.G., Nikitin, V.P., Shilova, G.N., 1983. New data on the sand strata of the Tuostakh Depression. [In Russian.] *Byuleten' Komiss. po Izucheniyu Chetvertichnogo Perioda AN SSSR* **52**, 107–122.

Kasse, C., 1997. Cold-climate aeolian sand-sheet formation in North-western Europe (*c.* 14–12.4 ka); a response to permafrost degradation and increased aridity. *Permafrost and Periglacial Processes* **8**, 295–311.

Kasse, C., 2002. Sandy aeolian deposits and environments and their relation to climate during the Last Glacial Maximum and Lateglacial in northwest and central Europe. *Progress in Physical Geography* **26**, 507–532.

Kasse, C., Aalbersberg, G., 2019. A complete Late Weichselian and Holocene record of aeolian coversands, drift sands and soils forced by climate change and human impact, Ossendrecht, the Netherlands. *Netherlands Journal of Geosciences* **98**, e4. https://doi.org/10.1017/njg.2019.3

Kasse, C., Vandenberghe, D., De Corte, F., Van den Haute, P., 2007. Late Weichselian fluvio–aeolian sands and coversand of the type locality Grubbenvorst (southern Netherlands): sedimentary environments, climate record and age. *Journal of Quaternary Science* **22**, 695–708.

Katasonov, E.M., Ivanov, M.S., 1973. *Cryolithology of Central Yakutia. Guide to Field Excursion Along the Lena and Aldan Rivers*. [In Russian.] Yakutsk Permafrost Institute, Siberian Branch, Academy of Sciences of the USSR, 37 pp.

Korotyaev, B.A., 2020. A review of weevils of the genus *Ceutorhynchus* (Coleoptera: Curculionidae), associated with woodland draba, *Draba nemorosa* (Brassicaceae). *Zoosystematica Rossica* **29**, 353–367.

Koster, E.A., 1988. Ancient and modern cold-climate aeolian sand deposition: a review. *Journal of Quaternary Research* **3**, 69–83.

Lea, P.D., 1990. Pleistocene periglacial eolian deposits in southwestern Alaska: sedimentary facies and depositional processes. *Journal of Sedimentary Petrology* **60**, 582–591.

Lea, P.D., Waythomas, C.F., 1990. Late-Pleistocene eolian sand sheets in Alaska. *Quaternary Research* **34**, 269–281.

Lee, E.J., Merriwether, D.A., Kasparov, A.K., Nikolskiy, P.A., Sotnikova, M.V., Pavlova, E.Y., Pitulko, V.V., 2015. Ancient DNA analysis of the oldest canid species from the Siberian Arctic and genetic contribution to the domestic dog. *PLoS ONE* **10**, e0125759. https://doi.org/10.1371/journal.pone.0125759

Lozhkin, A.V., Anderson, P.M., Matrosova, T.V., Minyuk, P.S., 2007. The pollen record from El'gygytgyn Lake: implications for vegetation and climate histories of northern Chukotka since the late middle Pleistocene. *Journal of Paleolimnology* **37**, 135–153.

Lukyanycheva, M.S., Kurbanov, R.N., Taratunina, N.A., Vasilieva, A.N., Lytkin, V.M., Panin, A.V., Anoikin, A.A., *et al.*, 2024. Dating post-LGM aeolian sedimentation and the Late Palaeolithic in Central Yakutia (northeastern Siberia). *Quaternary Geochronology* **83**, 101563. https://doi.org/10.1016/j.quageo.2024.101563

McGee, D., Broecker, W.S., Winckler, G., 2010. Gustiness: the driver of glacial dustiness? *Quaternary Science Reviews* **29**, 2340–2350.

Melles, M., Brigham-Grette, J., Glushkova, O.Y., Minyuk, P.S., Nowaczyk, N.R., Hubberten, H.W., 2007. Sedimentary geochemistry of core PG1351 from Lake El'gygytgyn—a sensitive record of climate variability in the East Siberian Arctic during the past three glacial–interglacial cycles. *Journal of Paleolimnology* **37**, 89–104.

Meyer, H., Schönicke, L., Wand, U., Hubberten, H.-W., Friedrichsen, H., 2000. Isotope studies of hydrogen and oxygen in ground ice – experiences with the equilibration technique. *Isotopes in Environmental and Health Studies* **36**, 133–149.

Minyuk, P.S., Ivanov, Y.Y., 2011. The Bruhnes–Matuyama boundary in Western Beringia: a review. *Quaternary Science Reviews* **30**, 2054–2068.

Mollenhauer, G., Grotheer, H., Gentz, T., Bonk, E., Hefter, J., 2021. Standard operation procedures and performance of the MICADAS radiocarbon laboratory at Alfred Wegener Institute (AWI), Germany. *Nuclear Instruments and Methods in Physics Research Section B: Beam Interactions with Materials and Atoms* **496**, 45–51.

Murton, J.B., Bateman, M.D., 2007. Syngenetic sand veins and anti-syngenetic sand wedges, Tuktoyaktuk Coastlands, western Arctic Canada. *Permafrost and Periglacial Processes* **18**, 33–47.

Murton, J.B., Edwards, M.E., Lozhkin, A.V., Anderson, P.M., Savvinov, G.N., Bakulina, N., Bondarenko, O.V., *et al.*, 2017. Preliminary palaeoenvironmental analysis of permafrost deposits at Batagaika megaslump, Yana Uplands, northern Siberia. *Quaternary Research* **87**, 314–330.

Murton, J.B., Goslar, T., Edwards, M.E., Bateman, M.D., Danilov, P.P., Savvinov, G.N., Gubin, S.V., *et al.*, 2015. Palaeoenvironmental interpretation of yedoma silt (ice complex) deposition as cold-climate loess, Duvanny Yar, northeast Siberia. *Permafrost and Periglacial Processes* **26**, 207–288.

Murton, J.B., Opel, T., Toms, P., Blinov, A., Fuchs, M., Wood, J., Gärtner, A., *et al.*, 2022. A multi-method dating study of ancient permafrost, Batagay megaslump, east Siberia. *Quaternary Research* **105**, 1–22.

Murton, J.B., Opel, T., Wetterich, S., Ashastina, K., Savvinov, G.G., Danilov, P.P., Boeskorov, V., 2023. Batagay megaslump: a review of the permafrost deposits, Quaternary environmental history, and recent development. *Permafrost and Periglacial Processes* **34**, 399–416.

Niessen, F., Hong, J.K., Hegewald, A., Matthiessen, J., Stein, R., Kim, H., Kim, S., *et al.*, 2013. Repeated Pleistocene glaciation of the East Siberian continental margin. *Nature Geoscience* **6**, 842–846.

https://doi.org/10.1017/qua.2024.36 Published online by Cambridge University Press

Nikolskiy, P.A., 2010. Systematics and Stratigraphic Significance of Late Cenozoic Elk/Moose (Alcini, Cervidae, Mammalia) from Eurasia and North America. [In Russian.] PhD thesis, Geological Institute of the Russian Academy of Sciences, Moscow, Russia.

Nikolskiy, P.A., Basilyan, A.E., Zazhigin, V.S., 2017. New data on the age of the glaciation in the New Siberian Islands (Russian Eastern Arctic). *Doklady Earth Sciences* **475**, 748–752.

Nugteren, G., Vandenberghe, J., 2004. Spatial climatic variability on the Central Loess Plateau (China) as recorded by grain size for the last 250 kyr. *Global and Planetary Change* **41**, 185–206.

Opel, T., Murton, J.B., Wetterich, S., Meyer, H., Ashastina, K., Günther, F., Grotheer, H., *et al.*, 2019. Past climate and continentality inferred from ice wedges at Batagay megaslump in the Northern Hemisphere's most continental region, Yana Highlands, interior Yakutia. *Climate of the Past* **15**, 1443–1461.

Opel, T., Wetterich, S., Meyer, H., Dereviagin, A.Y., Fuchs, M.C., Schirrmeister, L., 2017. Ground-ice stable isotopes and cryostratigraphy reflect late Quaternary palaeoclimate in the Northeast Siberian Arctic (Oyogos Yar coast, Dmitry Laptev Strait). *Climate of the Past* **13**, 587–611.

Péwé, T.L., Journaux, A., 1983. *Origin and Character of Loess-like Silt in Unglaciated South-Central Yakutia, Siberia, U.S.S.R.* United States Geological Survey Professional Paper 1262, Washington, DC. https://doi.org/10.3133/pp1262

Péwé, T.L., Journaux, A., Stuckenrath, R., 1977. Radiocarbon dates and Late-Quaternary stratigraphy from Mamontova Gora, unglaciated central Yakutia, Siberia, U.S.S.R. *Quaternary Research* **8**, 51–63.

Péwé, T.L., Westgate, J.A., Preece, S.J., Brown, P.M., Leavitt, S.W., 2009. Late Pliocene Dawson Cut Forest Bed and new tephrochronological findings in the Gold Hill Loess, east-central Alaska. *Geological Society of America Bulletin* **121**, 294–320.

Pissart, A., Vincent, J-S., Edlund, S.A., 1977. Dépôts et phenomènes éoliens sur L'île de Banks, Territoires du Nort-Ouest, Canada. *Canadian Journal of Earth Sciences* **14**, 2462–2480.

Porter, T.J., Opel, T., 2020. Recent advances in paleoclimatological studies of Arctic wedge- and pore-ice stable-water isotope records. *Permafrost and Periglacial Processes* **31**, 429–441.

Rampton, V.N., 1988. *Quaternary Geology of the Tuktoyaktuk Coastlands*. Memoir 423. Geological Survey of Canada, Ottawa, Ontario.

Reimer, P., Austin, W.E.N., Bard, E., Bayliss, A., Blackwell, P.G., Bronk Ramsey, C., Butzin, M., *et al.*, 2020. The IntCal20 Northern Hemisphere radiocarbon age calibration curve (0–55 cal kBP). *Radiocarbon* **62**, 725–757.

Reimer, P.J., Brown, T.A., Reimer, R.W., 2004. Discussion: Reporting and calibration of post-bomb C-14 data. *Radiocarbon* **46**, 1299–1304.

Reyes, A.V., Jensen, B.J., Woudstra, S.H., Bolton, M.S.M., Buryak, S.D., Cook, M.S., Harvey, J., Westgate, J.A., 2023. Detrital glass in a Bering Sea sediment core yields a ca. 160 ka Marine Isotope Stage 6 age for Old Crow tephra. *Geology* **51**, 106–110.

Reyes, A.V., Jensen, B.J., Zazula, G.D., Ager, T.A., Kuzmina, S., La Farge, C., Froese, D.G., 2010. A late–Middle Pleistocene (Marine Isotope Stage 6) vegetated surface buried by Old Crow tephra at the Palisades, interior Alaska. *Quaternary Science Reviews* **29**, 801–811.

Rhodes, E.J., 2015. Dating sediments using potassium feldspar single-grain IRSL: initial methodological considerations. *Quaternary International* **362**, 14–22.

Ruegg, G.H.J., 1983. Periglacial eolian evenly laminated sandy deposits in the Late Pleistocene of NW Europe, a facies unrecorded in modern sedimentological handbooks. In: Brookfield, M.E., Ahlbrandt, T.S. (Eds.), *Eolian Sediment and Processes*. Elsevier, Amsterdam, pp. 455–482.

Sambrook Smith, G.H., Ashworth, P.J., Best, J.L., Woodward, J., Simpson, C.J., 2006. The sedimentology and alluvial architecture of the sandy braided South Saskatchewan River, Canada. *Sedimentology* **53**, 413–434.

Schirrmeister, L., Dietze, E., Matthes, H., Grosse, G., Strauss, J., Laboor, S., Ulrich, M., Kienast, F., Wetterich, S., 2020. The genesis of Yedoma Ice Complex permafrost – grain-size endmember modeling analysis from Siberia and Alaska. *E&G Quaternary Science Journal* **69**, 33–53.

Schirrmeister, L., Froese, D., Wetterich, S., Strauss, J., Veremeeva, A., Grosse, G., 2025. Yedoma: Late Pleistocene ice-rich syngenetic permafrost of Beringia. In: Elias, S.A. (Ed.), *Encyclopedia of Quaternary Science: Third Edition*. Vol. 5. Elsevier, Amsterdam, pp. 296–311.

Schokker, J., Koster, E.A., 2004. Sedimentology and facies distribution of Pleistocene cold-climate aeolian and fluvial deposits in the Roer Valley Graben (southeastern Netherlands). *Permafrost and Periglacial Processes* **15**, 1–20.

Schwan, J., 1986. The origin of horizontal alternating bedding in Weichselian aeolian sands in northwestern Europe. *Sedimentary Geology* **49**, 73–108.

Schwan, J., 1988. The structure and genesis of Weichselian to early Holocene aeolian sand sheets in western Europe. *Sedimentary Geology* **55**, 197–232.

Sher, A., Kuzmina, S., 2013. Late Pleistocene of Northern Asia. In: Elias, S.A., Mock, C.J. (Eds.), *Encyclopedia of Quaternary Science: Second Edition*. Vol. 2. Elsevier, Amsterdam, pp. 255–273.

Sher, A.V., Weinstock, J., Baryshnikov, G.F., Davydov, S.P., Boeskorov, G.G., Zazhigin, V.S., Nikolskiy, P.A., 2011. The first record of "spelaeoid" bears in Arctic Siberia. *Quaternary Science Reviews* **30**, 2238–2249.

Skelly, R.L., Bristow, C.S., Ethridge, F.G., 2003. Architecture of channel-belt deposits in an aggrading shallow sandbed braided river: the lower Niobrara River, northeast Nebraska. *Sedimentary Geology* **158**, 249–270.

Squyres, S.W., Andersen, D.W., Nedell, S.S., Wharton, R.A., Jr., 1991. Lake Hoare, Antarctica: sedimentation through a thick perennial ice cover. *Sedimentology* **38**, 363–379.

Stuiver, M., Reimer, P., 1993. Extended ^{14}C data base and revised CALIB 3.0 ^{14}C age calibration program. *Radiocarbon* **35**, 215–230.

Sun, Y., An, Z., 2005. Late Pliocene-Pleistocene changes in mass accumulation rates of eolian deposits on the central Chinese Loess Plateau. *Journal of Geophysical Research* **110**, D23101. https://doi:10.1029/2005JD006064

Tomirdiaro, S.V., 1980. *Loess-Ice Formation of East Siberia in Late Pleistocene and Holocene*. [In Russian.] Nauka, Moscow.

Tomirdiaro, S.V., 1982. Evolution of lowland landscapes in northern Asia during Late Quaternary time. In: Hopkins, D.M., Matthews, J.V., Jr., Schweger, C.E., Young, S.B. (Eds.), *Paleoecology of Beringia*. Academic Press, New York, pp. 29–37.

Tomskaya, A.I., Savvinova, G.M., 1971. Spore–pollen spectra of Pleistocene deposits of the middle Yana River basin. In: *Palynological Characteristics of Paleozoic, Mesozoic and Cenozoic Deposits of Yakutia*. [In Russian.] Kn. izdvol, Yakutsk.

Torgovkin, N.V., Sivtsev, D.E., Gavrilova, A.A., Platonov, I.A., Kizyakov, A.I., Schirrmeister. L., Opel, T., Wetterich, S., Breitenbach, S.F.M., Meyer, H., 2024. New data on the geochronology of Quaternary sediments and stable oxygen and hydrogen isotopes in ground ice of the Mamontova Gora. [In Russian.] *Kriozfera Zemlii* [Earth's Cryosphere] **28**, 3–13.

Tumskoy, V.E., 2012. Osobennosti Kriolitogeneza Otlozheniy Severnoi Yakutii V Srednem Pleistotsene – Golotsene [Peculiarities of cryolithogenesis of deposits in northern Yakutia in the Middle Neopleistocene–Holocene]. *Kriozfera Zemlii* [Earth's Cryosphere] **XVI**(1), 12–21.

Tumskoy, V.E., Kuznetsova, T.V., 2022. Cryolithostratigraphy of the Middle Pleistocene to Holocene deposits in the Dmitry Laptev Strait, Northern Yakutia. *Frontiers in Earth Science* **10**, 789421. https://doi.org/10.3389/feart.2022.789421

USSR Climate Digest, 1989. Issue 24, Yakutskaya ASSR. Chast 3. Veter i atmosphernoe davlenie. Red.vyp. Smirnova, N.S. Yakutskij Gidrometeorologicheskij Zentr, Yakutsk.

Vandenberghe, J., van Huissteden, J., 1988. Fluvial–aeolian interaction in a region of continuous permafrost. In: Senneset, K. (Ed.), *Proceedings of the Fifth International Conference on Permafrost, Trondheim, Norway, 2–5 August 1988*. Vol. 1. Tapir Publishers, Trondheim, Norway, pp. 876–881.

Vangengeim, E.A., 1961. Palaeontologic evidence for stratigraphy of anthropogenic deposits in the North of Eastern Siberia. [In Russian.] *Proceedings of the Geological Institute, USSR Academy of Sciences* **48**, 183 pp.

Van Huissteden, J., Vandenberghe, J., Van der Hammen, T., Laan, W., 2000. Fluvial and aeolian interaction under permafrost conditions: Weichselian Late Pleniglacial, Twente, eastern Netherlands. *Catena* **40**, 307–321.

Vdovina, L.G., 2002a. *Map of Quaternary Formations. Report on Geological Survey, Re-compilation and Preparation for Publication of the State Map of the Russian Federation (Russia) at a scale of* 1:200 000 (*New series*) *sheet Q-53-III,IV [Batagai (Ege-Haya)] in* 1995–2001. [In Russian.] Annex 7 Sheet. State Committee of the Republic of Sakha (Yakutia) on Geology and Subsoil Use of the Order of Honour State Unitary Mining and Geological Enterprise Yangheologiya.

https://doi.org/10.1017/qua.2024.36 Published online by Cambridge University Press

Vdovina, L.G., 2002b. *Geological Map. Report on Geological Survey, Re-compilation and Preparation for Publication of the State Map of the Russian Federation* (*Russia*) *at a scale of* 1:200 000 (*New series*) *sheet Q-53-III,IV [Batagai* (*Ege-Haya*)*] in* 1995–2001. [In Russian.] Annex 2 Sheet. State Committee of the Republic of Sakha (Yakutia) on Geology and Subsoil Use of the Order of Honour State Unitary Mining and Geological Enterprise Yangheologiya.

Vdovina, L.G., Skuba, V.D., 2013a. State Geological Map of Russia at a Scale of 1:200,000 (Second edition). Verkhoyanskaya Series. Sheet Q-53-III, IV (Batagay). [In Russian.] Russian Geological Research Institute (VSEGEI), Moscow.

Vdovina, L.G., Skuba, V.D., 2013b. In: Senotrusov, Y.I., Fedyanin, A.N. (Eds.), *Explanatory Note*. State Geological Map of Russia at a Scale of 1:200,000 (Second edition). Verkhoyanskaya Series. Sheet Q-53-III, IV (Batagay). [In Russian.] Russian Geological Research Institute (VSEGEI), Moscow.

Wang, X., Ma, J., Yi, S., Vandenberghe, J., Dai, Y., Lu, H., 2019. Interaction of fluvial and eolian sedimentation processes, and response to climate change since the last glacial in a semiarid environment along the Yellow River. *Quaternary Research* **91**, 570–583.

Wennrich, V., Andreev, A.A., Tarasov, P.E., Fedorov, G., Zhao, W., Gebhardt, C.A., Meyer-Jacob, C., *et al.*, 2016. Impact processes, permafrost dynamics, and climate and environmental variability in the terrestrial Arctic as inferred from the unique 3.6 Myr record of Lake El'gygytgyn, Far East Russia—a review. *Quaternary Science Reviews* **147**, 221–244.

Wetterich, S., Meyer, H., Fritz, M., Mollenhauer, G., Rethemeyer, J., Kizyakov, A., Schirrmeister, L., Opel, T., 2021. Northeast Siberian permafrost ice-wedge stable isotopes depict pronounced Last Glacial Maximum winter cooling. *Geophysical Research Letters* **48**, e2020GL092087. https://doi.org/10.1029/2020GL092087

Wetterich, S., Rudaya, N., Kuznetsov, V., Maksimov, F., Opel, T., Meyer, H., Günther, F., *et al.*, 2019. Ice complex formation on Bol'shoy Lyakhovsky Island (New Siberian Archipelago, East Siberian Arctic) since about 200 ka. *Quaternary Research* **92**, 530–548.

Wetterich, S., Rudaya, N., Tumskoy, V., Andreev, A.A., Opel, T., Schirrmeister, L., Meyer, H., 2011. Last Glacial Maximum records in permafrost of the East Siberian Arctic. *Quaternary Science Reviews* **30**, 3139–3151. https://doi.org/10.1016/j.quascirev.2011.07.020

Wetterich, S., Tumskoy, V., Rudaya, N., Kuznetsov, V., Maksimov, F., Opel, T., Meyer, H., Andreev, A.A., Schirrmeister, L., 2016. Ice complex permafrost of MIS5 age in the Dmitry Laptev Strait coastal region (East Siberian Arctic). *Quaternary Science Reviews* **147**, 298–311.

Wintle, A.G., Murray, A.S., 2006. A review of quartz optically stimulated luminescence characteristics and their relevance in single-aliquot regeneration dating protocols. *Radiation Measurements* **4**, 369–391.

Worsley, P., 2015. Late Pleistocene geology of the Chelford area of Cheshire. *Mercian Geologist* **18**, 202–212.

Zaretskaya, N., Panin, A., Utkina, A., Baranov, D., 2024. Aeolian sedimentation in the Vychegda river valley, north-eastern Europe, during MIS 2–1. *Quaternary International* **686–687**, 83–98.

Zech, M., Zech, R., Zech, W., Glaser, B., Brodowski, S., Amelung, W., 2008. Characterisation and palaeoclimate of a loess-like permafrost palaeosol sequence in NE Siberia. *Geoderma* **143**, 281–295.

Zhao, W., Andreev, A.A., Wennrich, V., Li, Q., Melles, M., 2022. Quaternary environmental changes in central Chukotka (NE Russia) inferred from the Lake El'gygytgyn pollen records. *Journal of Quaternary Science* **37**, 915–927.

Zhong, Y., Liu, Y., Yang, H., Yin, Q., Wilson, D.J., Lu, Z., Jaccard, S.L., *et al.*, 2024. Orbital controls on North Pacific dust flux during the late Quaternary. *Geophysical Research Letters* **51**, e2023GL106631. https://doi.org/10.1029/2023GL106631

https://doi.org/10.1017/qua.2024.36 Published online by Cambridge University Press